

## Dynamic Spin Correlations in the Honeycomb Lattice $\text{Na}_2\text{IrO}_3$ Measured by Resonant Inelastic x-Ray Scattering

Jungho Kim<sup>1,\*</sup>, Jiří Chaloupka<sup>2,3,†</sup>, Yogesh Singh,<sup>4</sup> J. W. Kim,<sup>1</sup> B. J. Kim,<sup>5,6</sup> D. Casa,<sup>1</sup> A. Said,<sup>1</sup> X. Huang,<sup>1</sup> and T. Gog<sup>1</sup>

<sup>1</sup>Advanced Photon Source, Argonne National Laboratory, Argonne, Illinois 60439, USA

<sup>2</sup>Central European Institute of Technology, Masaryk University, Kamenice 753/5, CZ-62500 Brno, Czech Republic

<sup>3</sup>Department of Condensed Matter Physics, Faculty of Science, Masaryk University, Kotlářská 2, CZ-61137 Brno, Czech Republic

<sup>4</sup>Department of Physical Sciences, Indian Institute of Science Education and Research Mohali, Knowledge City, Sector 81, Mohali 140306, India

<sup>5</sup>Department of Physics, Pohang University of Science and Technology, Pohang 790-784, Republic of Korea

<sup>6</sup>Center for Artificial Low Dimensional Electronic Systems, Institute for Basic Science (IBS), 77 Cheongam-Ro, Pohang 790-784, Republic of Korea



(Received 16 April 2019; revised manuscript received 14 March 2020; accepted 23 March 2020; published 13 May 2020)

A Kitaev quantum spin liquid is a prime example of novel quantum magnetism of spin-orbit entangled pseudospin-1/2 moments in a honeycomb lattice. Most candidate materials such as  $\text{Na}_2\text{IrO}_3$  have many competing exchange interactions beyond the minimal Kitaev-Heisenberg model whose small variations in the strength of the interactions produce huge differences in low-energy dynamics. Our incomplete knowledge of dynamic spin correlations hampers identification of a minimal model and quantification of the proximity to the Kitaev quantum spin-liquid phase. Here, we report momentum- and energy-resolved magnetic excitation spectra in a honeycomb lattice  $\text{Na}_2\text{IrO}_3$  measured using a resonant inelastic x-ray scattering spectrometer capable of 12 meV resolution. Measured spectra at a low temperature show that the dynamic response lacks resolution-limited coherent spin waves in most parts of the Brillouin zone but has a discernible dispersion and spectral weight distribution within the energy window of 60 meV. A systematic investigation using the exact diagonalization method and direct comparison of high-resolution experimental spectra and theoretical simulations allow us to confine a parameter regime in which the extended Kitaev-Heisenberg model reasonably reproduces the main feature of the observed magnetic excitations. Hidden Kitaev quantum spin-liquid and Heisenberg phases found in the complex parameter space are used as references to propose the picture of renormalized magnons as explaining the incoherent nature of magnetic excitations. Magnetic excitation spectra are taken at elevated temperatures to follow the temperature evolution of the resonant inelastic x-ray scattering dynamic response in the paramagnetic state. Whereas the low-energy excitation progressively diminishes as the zigzag order disappears, the broad high-energy excitation maintains its spectral weight up to a much higher temperature of 160 K. We suggest that the dominant nearest-neighbor interactions keep short-range correlations up to quite high temperatures with a specific short-range dynamics which has a possible connection to a proximate spin-liquid phase.

DOI: [10.1103/PhysRevX.10.021034](https://doi.org/10.1103/PhysRevX.10.021034)

Subject Areas: Condensed Matter Physics, Magnetism, Strongly Correlated Materials

### I. INTRODUCTION

A Kitaev quantum spin liquid (KQSL) is a topological phase of matter resulting from an exactly solvable Hamiltonian of nearest-neighbor bond-directional interactions between half-integer spins in a honeycomb lattice [1,2]. Their long-range quantum entanglement and topologically protected fractional excitations are of particular interest for potential quantum computing platforms [3]. It has been pointed out that the bond-directional Kitaev

\*jhkim@aps.anl.gov

†chaloupka@physics.muni.cz

Published by the American Physical Society under the terms of the [Creative Commons Attribution 4.0 International license](https://creativecommons.org/licenses/by/4.0/). Further distribution of this work must maintain attribution to the author(s) and the published article's title, journal citation, and DOI.

interactions arise naturally in a honeycomb magnet with strong spin-orbit coupling, which triggered a wave of searching for a material realization of the KQSL [4]. The Kitaev-Heisenberg model and related spin models indicate extended stability of the spin-liquid phase away from the pure Kitaev limit [5–10], which widens the scope of candidate materials.

$\text{Na}_2\text{IrO}_3$  is one of the first and most extensively studied candidate materials despite having a conventional symmetry-breaking magnetic order as in other honeycomb magnets [11–14]. A zigzag antiferromagnetic (AFM) order was found by resonant x-ray magnetic scattering and inelastic neutron scattering [12–14]. It has been shown that the inclusion of small Heisenberg terms, omnipresent in all materials, can explain the zigzag order [13,14]. Subsequently, many other models were proposed which may be more realistic but are of increased complexity [6–10]. Resonant magnetic x-ray scattering measurements provide important constraints on the minimal model and the sign of the Kitaev term [15]. It was found that the ordered magnetic moment direction approximately bisects the angle between the cubic  $x$  and  $y$  axes and that two other dynamically fluctuating zigzag orders related to the static one by the approximate  $C_3$  symmetry of the lattice have their corresponding moment directions [15]. These results imply a dominant ferromagnetic Kitaev term ( $K$ ) with a non-negligible off-diagonal exchange ( $\Gamma$ ), which is supported by quantum chemistry [16] and other *ab initio* calculations [17,18]. The off-diagonal exchange which is symmetry allowed can be sizable when direct exchange is effective [7]. At a classical level, a spin-liquid phase is theoretically found in models with a large off-diagonal exchange [19]. The infinite density matrix renormalization group study on the  $K$ - $\Gamma$  model found strong numerical evidence for the existence of a quantum spin liquid for ferrolite Kitaev interactions [20].

The materials search for the KQSL led to the discovery of many other honeycomb materials [21–26]. For example,  $\text{Cu}_2\text{IrO}_3$  and hydrogen-intercalated  $\text{H}_3\text{LiIr}_2\text{O}_6$  are found to bear no sign of a magnetic order down to the lowest temperatures [24,25]. The  $4d$  compound  $\alpha\text{-RuCl}_3$  is found to be a  $J_{\text{eff}} = 1/2$  Mott insulator despite having a much smaller magnitude of spin-orbit coupling and has received much attention recently [26]. Dynamic spin correlations of  $\alpha\text{-RuCl}_3$  have been extensively studied by inelastic neutron scattering (INS) [27–30]. The dynamical structure factor through INS reveals a highly unusual intensity distribution over a large energy interval around the zone center [29,30]. Although incoherent excitations originating from strong magnetic anharmonicity can naturally occur in a highly anisotropic frustrated magnet [31,32], several theoretical works support that the broad feature is a dynamic response of Majorana fermions—a salient nonlocal feature of the Kitaev quantum spin-liquid phase [33–37].

Phenomenologically,  $\text{Na}_2\text{IrO}_3$  and  $\alpha\text{-RuCl}_3$  share several common features: an unusual broad continuum in their Raman scattering spectra [38,39]; magnetic entropy recovered or released in two widely separated temperature scales in heat capacity measurements [30,40]; and high-field evolution of the zigzag-ordered phase to a nonmagnetic phase in magnetic torque measurements [41,42]. However, measurement of the dynamical structure factor providing the most direct information thus far remains elusive for  $\text{Na}_2\text{IrO}_3$ , because resonant inelastic x-ray scattering (RIXS) suffers from insufficient energy resolution and INS is difficult for Ir compounds due to their high neutron absorption. The INS measurement on polycrystalline  $\text{Na}_2\text{IrO}_3$  samples at a low temperature observes spin-wave excitations with a sinusoidal-like low-momentum dispersion, which can be best understood by including substantial further-neighbor exchanges that stabilize the zigzag magnetic order [14]. Previous RIXS measurement on single-crystal  $\text{Na}_2\text{IrO}_3$  observed only a broad low-energy excitation interpreted as containing signals of magnetic and phonon origins [43], which limits a detailed comparison with theoretical calculations. A more recent RIXS measurement rules out the phonon interpretation of the low-energy excitation by showing different peak energies of isostructural  $\text{Na}_2\text{IrO}_3$  and  $\text{Li}_2\text{IrO}_3$  and suggests a magnetic origin of the broad excitation [44], which is phenomenologically similar to the unusual broad scattering in  $\alpha\text{-RuCl}_3$  [29,30]. Both RIXS works can observe only the broad excitation and do not provide detailed information on the magnetic ground state.

Here, we report magnetic excitation spectra in a honeycomb lattice  $\text{Na}_2\text{IrO}_3$  measured by the state-of-the-art RIXS spectrometer providing an unprecedented energy resolution of 12 meV. The measurements are carried out along all high-symmetry paths including the second Brillouin zone (BZ) center. The 25 meV resolution spectra at  $T = 7$  K reveal a discernible dispersion and spectral distribution within the energy window of 60 meV. The 12 meV resolution allows us to characterize the spectral width of the excitation peak and better define the low-energy excitation feature [45,46]. The zone center spectrum lacks a resolution-limited peak typical of a coherent collective excitation and has a broad feature only at high energy. The incoherent feature persists over the whole BZ. As approaching the zone boundary, a spectral weight shifts toward lower energy. Remarkably, a sharp collective excitation peak whose width is comparable to the spectrometer resolution is resolved at the  $K$  point of the honeycomb BZ. An exact diagonalization method on finite-size clusters is used to find the relevant parameter regime of the extended Kitaev-Heisenberg model which captures the main features of the measured magnetic excitation spectra at a low temperature in terms of spectral dispersion and intensity. Hidden KQSL and Heisenberg phases found in the complex parameter space of the model

provide useful references for the nature of the magnetic excitations appearing in the measured spectra. We present the temperature evolution of the RIXS dynamic response up to 280 K, which reveals an anomalous behavior of the broad high-energy excitation.

The paper is organized as follows: Section II presents experimental RIXS spectra at low temperatures. Section III describes the simulations of the low-temperature RIXS data based on the extended Kitaev-Heisenberg model and discusses the nature of the observed magnetic excitations. The zigzag phase of the model is systematically explored, and several kinds of differing pseudospin dynamics are observed. Comparing directly the experiment and theoretical RIXS spectra, this observation is used to identify the parameter regime consistent with the experimental data. A picture of renormalized magnons is proposed to explain the main spectral features in this regime. Section IV presents

experimental RIXS spectra at high temperatures and discusses the anomalous higher-energy spectral intensities in the context of Kitaev systems at a finite temperature. Section V concludes the paper and presents a perspective on a RIXS probe for higher-order correlations that detects the full continuum of the Majorana fermions of the QKSL. The Appendixes provide details of our experimental setup, the description of the numerical computations, and a discussion of the hidden-symmetry points of the extended Kitaev-Heisenberg model that are utilized in Sec. III.

## II. MAGNETIC EXCITATION SPECTRA AT A LOW TEMPERATURE

### A. RIXS scatterings over the entire Brillouin zone

Figure 1(d) shows a RIXS intensity map recorded at  $T = 7$  K along the  $\Gamma$ - $M$ - $\Gamma'$ - $X$ - $K$ - $\Gamma$ - $Y$ - $K'$ - $\Gamma'$  path of the in-plane

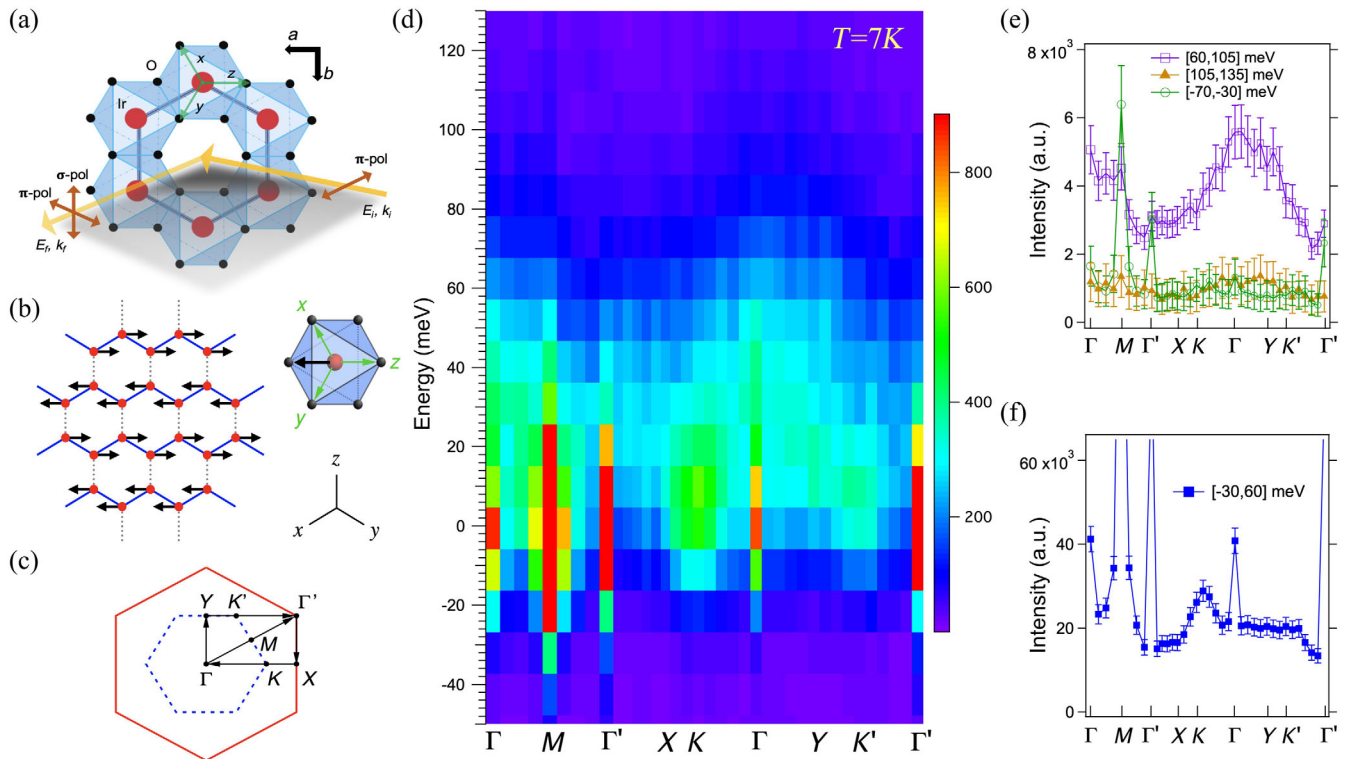


FIG. 1. Magnetic excitation spectra in  $\text{Na}_2\text{IrO}_3$  along high-symmetry Brillouin zone directions taken at  $T = 7$  K. (a) Scattering geometry. Yellow arrows indicate incident and scattered x rays, which define the scattering plane (gray). Brown arrows indicate x-ray polarizations. Green arrows indicate the cubic axes ( $x, y, z$ ) with respect to the octahedra (all of them point above the paper plane). (b) One of the collinear zigzag patterns and the corresponding direction of the ordered moments. The left-facing arrows have an out-of-plane component pointing above the paper plane; i.e., the corresponding moment direction lies approximately between the  $x$  and  $y$  axes. (c) Two-dimensional reciprocal space diagram showing the measured path along the symmetry directions. The inner hexagon (blue dashed line) indicates the first Brillouin zone of the honeycomb lattice. (d) RIXS intensity map of magnetic excitations in  $\text{Na}_2\text{IrO}_3$  as functions of the wave vector and energy loss. (e) The intensity profiles integrated over  $[60, 105]$  (open squares) and  $[105, 135]$  meV (filled triangles) show that the high-energy spectral intensities are broadly peaked at the  $\Gamma$  point, extending up to 105 meV. (f) The intensity profile integrated over  $[-30, 60]$  meV (filled squares) shows a distinctive distribution of the spectral weight along the  $K$ - $\Gamma$ - $Y$ - $K'$ - $\Gamma'$  path. Passing through the  $K$  point, the excitation intensity rapidly increases and then decreases, which is followed by a near-constant intensity along the  $\Gamma$ - $Y$ - $K'$  path. Large intensities at the  $\Gamma$  and  $\Gamma'$  wave vectors correspond to elastic scatterings. The zero-energy loss intensity at the  $M$  point is the diffuse magnetic Bragg peak. In the used scattering geometry, the magnetic Bragg peak at the  $Y$  point is suppressed.

momentum transfer as shown in Fig. 1(c). These RIXS spectra are obtained from a standard setup with conventional 25 meV resolution using a Si(844) diced spherical analyzer [47,48]. The out-of-plane momentum transfer is varied to keep the scattering angle close to  $90^\circ$  to minimize elastic scatterings. Singular intensities at zero energy loss at  $\Gamma$  ( $\Gamma'$ ) and  $M$  originate from a specular elastic scattering and a static zigzag magnetic order [11–14], respectively. Polarization factors in the current scattering geometry depicted in Fig. 1(a) lead to a vanishing magnetic Bragg peak at the  $Y$  point and a weak scattering intensity at the  $K'$  point relative to the  $K$  point [15].

The main dispersing feature is observed in the first BZ along the  $K$ - $\Gamma$ - $Y$ - $K'$  path below approximately 60 meV. An intense low-energy excitation around 10 meV is clearly seen near the  $K$  point. The spectral intensity moves to higher energy along the  $K$ - $\Gamma$  path, reaching its highest energy at the  $\Gamma$  point, and disperses toward lower energy along the  $\Gamma$ - $Y$ - $K'$  path.

For each wave vector, the intensity is integrated over an energy window of interest to obtain the distribution of the spectral weight in the BZ. Figure 1(e) shows the intensity profiles on the high-energy loss and the energy gain sides. The intensity over the far energy loss region ([105, 135] meV, filled triangles) shows a nearly constant value which is comparable to that of the far energy gain region ([−70, −30] meV, open circles). The intensity profile integrated over [60, 105] meV (open squares) in Fig. 1(f) shows a distribution, peaked broadly around the BZ center  $\Gamma$ . These indicate that the spectral intensity of the observed excitation extends roughly to 105 meV.

Figure 1(f) shows the intensity distribution of the main feature ([−30, 60] meV, filled squares) which reveals a distinctive distribution of the spectral weight as a function of the wave vector. Weak intensities are seen along the  $\Gamma'$ - $X$  line (outside the first Brillouin zone). Passing through the  $K$  point, the excitation intensity rapidly increases and then decreases, which is followed by a nearly constant intensity along the  $\Gamma$ - $Y$ - $K'$  path. The intensity is weakened as it approaches the  $\Gamma'$  point.

## B. High-energy resolution RIXS spectra

Recently, a higher energy resolution has been achieved for the Ir  $L_3$  RIXS by using the quartz(309) crystal [45,46]. In this work, the high-resolution quartz analyzer is used to better examine spectral widths of magnetic excitations at the  $\Gamma$ , near  $M$ ,  $Y$ , and  $K$  wave vectors, where prominent low-energy spectral weights below 20 meV are seen from the 25 meV RIXS spectra in Fig. 1(d). The measured energy resolution function of the quartz analyzer is plotted at the bottom in Fig. 2(a), which can be described with the pseudo-Voigt function with a 12 meV full width at half maximum (FWHM).

Strong elastic scatterings at  $\mathbf{Q} = (00\ 6.75)$  ( $\Gamma$ ) and  $(0.45\ 6.5)$  (near  $M$ ) are due to a specular scattering and a

quasielastic scattering due to the diffuse magnetic peak, respectively. At both wave vectors, resolution-limited peaks characteristic of coherent spin waves are not found, but broad incoherent scatterings are seen at high energies. At the  $\Gamma$ , the broad incoherent scattering has a clear peak structure at around 40 meV. At  $\mathbf{Q} = (0\ 1\ 6.5)$  ( $Y$ ), a glimpse of a low-energy peak is detected, and a broad peak is centered around 50 meV. On the other hand, a narrow width peak below 20 meV is clearly revealed at the  $\mathbf{Q} = (0.67\ 0\ 6.6)$  ( $K$ ) point, which is also followed by a broad feature.

Figure 2(b) shows the  $\Gamma$  point spectrum with a fit in which the elastic peak is fitted to the pseudo-Voigt resolution function and the broad incoherent peak is fitted by a damped harmonic oscillator (DHO) function convoluted by the pseudo-Voigt resolution function. Note that the high-resolution data have rather a large ratio of background to signal and poor statistics. The background level is determined in a way that the energy gain data below −30 meV are distributed around the zero, and such a background is subtracted from the raw data. The DHO function is expressed as  $An(T)\gamma\{1/[(E - E_0)^2 + \gamma^2] - 1/[(E + E_0)^2 + \gamma^2]\}$ , where  $A$  is the amplitude,  $n(T)$  is the Bose factor,  $E_0$  is the peak energy, and  $\gamma$  is the peak width. The fitted curves are overlaid with the  $\Gamma$  point data in Fig. 2(b). A damped peak of  $(E_0, \gamma) = (36, 22)$  meV is used to describe the broad incoherent peak. Figure 2(c) shows the  $K$  point spectrum, where the background level estimated for the  $\Gamma$  spectrum is assumed. The low-energy peak is described by a narrow width peak of  $(E_0, \gamma) = (3, 7)$  meV. The broad feature is fit by the  $(E_0, \gamma) = (38, 20)$  meV DHO.

Figure 2(d) shows the temperature dependence of the high-resolution RIXS spectrum at the  $K$  point.  $\text{Na}_2\text{IrO}_3$  is a Mott-like correlated insulator with a 340 meV energy gap [49]. Within the Mott gap of 340 meV, the lattice and spin degrees of freedom could be associated with the appearance of excitations. The temperature dependence data in Fig. 2(d), for example, provide a means to distinguish excitations of distinct origins. If the lattice degree of freedom is involved, the Bose population factor leads to an increasing intensity with an increasing temperature. On the other hand, at a temperature above a characteristic spin exchange energy, the contribution of the spin degree of freedom vanishes.

The low-energy peak in Fig. 2(d) clearly decreases at  $T = 70$  K and becomes featureless at  $T = 150$  K. The long-range zigzag order disappears above 15 K, but the diffuse magnetic scattering study finds that the short-range zigzag correlations survive at least up to 70 K [15]. Thus, this temperature dependence data establish that the low-energy peak is a magnon peak of the zigzag magnetic order. On the other hand, the broad feature intensity barely changes between 7 and 150 K. This observation is in contrast to the previous RIXS study [43], which finds a temperature-dependent broad scattering and interprets it as a resonant phonon contribution. However, a more recent

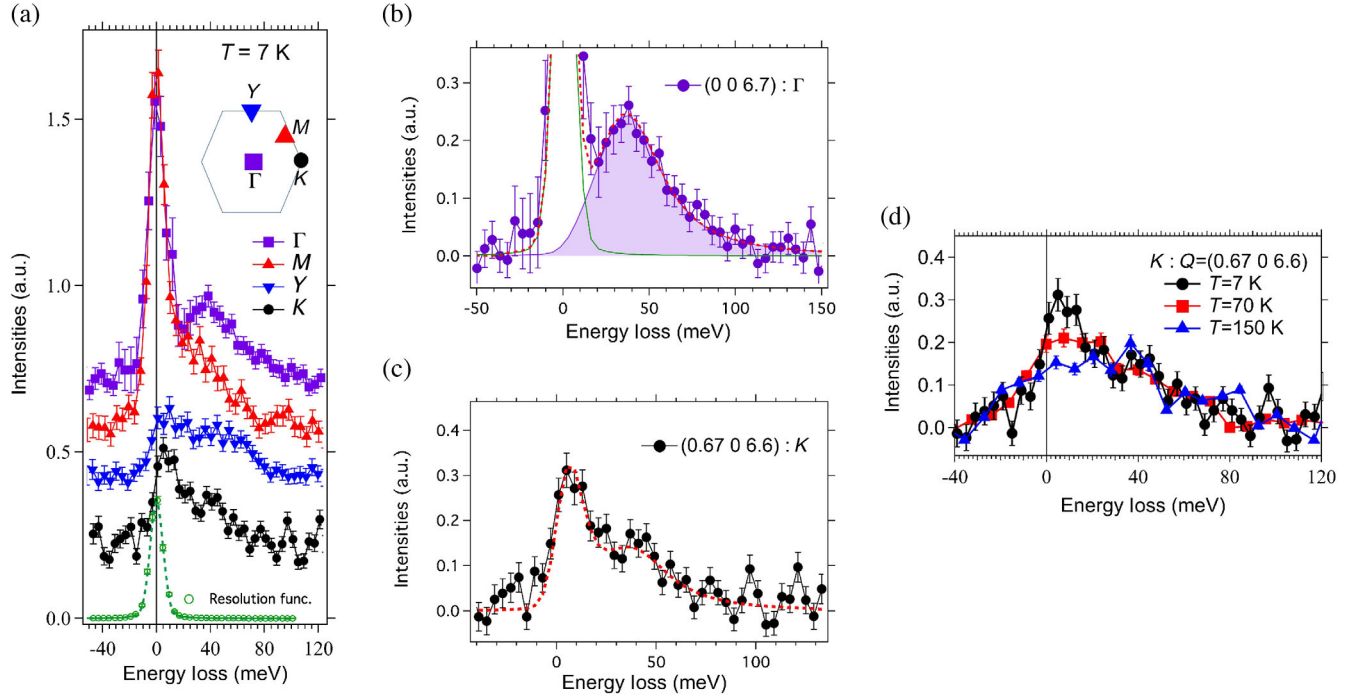


FIG. 2. High-resolution RIXS spectra recorded at  $T = 7$  K. (a) The measured energy resolution function of the quartz analyzer is plotted at the bottom. At  $\mathbf{Q} = (0\ 0\ 6.75)$  ( $\Gamma$ ), an elastic scattering is followed by a broad excitation without any indication of a narrow excitation. At  $\mathbf{Q} = (0.45\ 0.45\ 6.5)$  (near  $M$ ), a soft low-energy excitation is unresolved with 12 meV energy resolution, and a quasielastic scattering is followed by a broad shoulder excitation. At  $\mathbf{Q} = (0\ 1\ 6.5)$  ( $Y$ ), a low-energy excitation is seen with a broad high-energy feature. At  $\mathbf{Q} = (0.67\ 0\ 6.6)$  ( $K$ ), a narrow excitation is discovered at a low energy. (b),(c) The measured RIXS spectra at the  $\Gamma$  and  $K$  wave vectors, respectively, are fit by the pseudo-Voigt function (elastic scattering) and damped harmonic oscillator (DHO) function convoluted by the 12 meV resolution function. (d) Temperature dependence of the RIXS excitation spectrum at the  $K$  point. The low-energy peak shows a clear decrease at  $T = 70$  K and becomes featureless at  $T = 150$  K, indicating that it is an excitation peak of the zigzag magnetic order.

RIXS [44] reports that the broad scattering intensity hardly changes between 5 and 90 K and persists up to 300 K, which is consistent with the current observation. This recent RIXS work rules out the phonon interpretation of the low-energy excitation and claims the magnetic origin of the broad scattering intensity by showing different peak energies of isostructural  $\text{Na}_2\text{IrO}_3$  and  $\text{Li}_2\text{IrO}_3$  and the same resonance behavior of all low-energy signals [44]. Here, we assign the broad feature as having a magnetic origin and discuss in more detail in the next two sections.

### III. MODEL DESCRIPTION OF THE LOW- $T$ RIXS SPECTRA

#### A. Spin Hamiltonian

To perform a quantitative model analysis of the magnetic excitations as observed by RIXS, we adopt the extended Kitaev-Heisenberg model for  $J_{\text{eff}} = 1/2$  pseudospins [7,16,50]. Compared to the originally proposed Kitaev-Heisenberg model for  $\text{Na}_2\text{IrO}_3$  [4] comprising a dominant Kitaev interaction supplemented by a smaller Heisenberg interaction, the model is extended by two kinds of

off-diagonal exchange interactions. The nearest-neighbor Hamiltonian for the pseudospins  $\mathbf{S}$  then takes the form

$$\mathcal{H}_{ij}^{(z)} = K S_i^z S_j^z + J \mathbf{S}_i \cdot \mathbf{S}_j + \Gamma (S_i^x S_j^y + S_i^y S_j^x) + \Gamma' (S_i^x S_j^z + S_i^z S_j^x + S_i^y S_j^z + S_i^z S_j^y) \quad (1)$$

shown here for a  $z$  bond [vertical bond in Fig. 1(b); the bond direction is perpendicular to the  $z$  axis]. In the case of the other bond directions, a cyclic permutation of the pseudospin components is applied. Various *ab initio* estimates of the interaction parameters (e.g., Refs. [8,16,17]) generally suggest a dominant ferromagnetic (FM) Kitaev interaction ( $K < 0$ ) and a positive off-diagonal  $\Gamma$  interaction. This parameter setup, combined with suitable values of the smaller interaction parameters  $J$  and  $\Gamma'$ , favors the zigzag magnetic order with the magnetic moments pointing approximately in between the  $x$  and  $y$  axes (assuming the zigzag order with FM  $x$  and  $y$  bonds) which corresponds to the experimental situation [15]. In addition, motivated by sizable further-neighbor interactions found by the *ab initio* estimates (see, e.g., Ref. [17]), we also include isotropic

Heisenberg interactions among second and third nearest neighbors and arrive at the full model Hamiltonian

$$\mathcal{H} = \sum_{\langle ij \rangle \in \text{NN}} \mathcal{H}_{ij}^{(\gamma)} + \sum_{\langle ij \rangle \in 2^{\text{nd}} \text{NN}} J_2 \mathbf{S}_i \cdot \mathbf{S}_j + \sum_{\langle ij \rangle \in 3^{\text{rd}} \text{NN}} J_3 \mathbf{S}_i \cdot \mathbf{S}_j, \quad (2)$$

where  $\gamma$  labels the nearest-neighbor (NN) bond direction. Following the prevailing expectations, in our analysis we assume that the main interactions are  $K$ ,  $\Gamma$ , and  $J$ , while  $\Gamma'$ ,  $J_2$ , and  $J_3$  are significantly smaller in magnitude.

## B. Simulations of the low-temperature RIXS data

We simulate the RIXS spectra by calculating the dynamical pseudospin structure factor and combining its components according to the recipes given in Refs. [51,52]. Namely, we utilize the effective RIXS operator expressed within the Kramers doublet manifold via

$$\mathcal{R} \propto i(\boldsymbol{\varepsilon} \times \boldsymbol{\varepsilon}') \cdot (f_{ab} \mathbf{S}_{ab} + f_{\perp} \mathbf{S}_{\perp}). \quad (3)$$

Here,  $\boldsymbol{\varepsilon}$  and  $\boldsymbol{\varepsilon}'$  are the polarization vectors of the incident and scattered x rays, respectively, and  $\mathbf{S}_{ab}$  and  $\mathbf{S}_{\perp}$  denote the component of the pseudospin lying within the honeycomb plane (crystallographic  $ab$ ) and being perpendicular to it, respectively. For the  $L_3$  edge resonant process, the factors connecting the pseudospin and the RIXS operators read as  $f_{ab} = \frac{1}{2} + (5/6\sqrt{2}) \sin 2\vartheta - \frac{1}{6} \cos 2\vartheta$  and  $f_{\perp} = 1 + \frac{2}{3} \cos 2\vartheta - (1/3\sqrt{2}) \sin 2\vartheta$  with the angle  $\tan 2\vartheta = 2\sqrt{2}/(1 + 2\Delta/\lambda)$  being determined by the ratio of the trigonal field  $\Delta$  and the spin-orbit coupling constant  $\lambda$  [51,52]. The values of  $\vartheta$  for  $\text{Na}_2\text{IrO}_3$  can be estimated from the splitting  $\Delta_{BC} \approx 0.1$  eV of the  $J_{\text{eff}} = 3/2$  quartet [53], leading to slightly anisotropic  $f_{ab} \approx 0.91$  and  $f_{\perp} \approx 1.15$ .

The RIXS intensity is then calculated as the dynamical correlation function of the  $\mathcal{R}$  operator:  $I(\mathbf{q}, \omega) \propto \chi''_{\mathcal{R}}(\mathbf{q}, \omega)$  with  $\chi_{\mathcal{R}}(\mathbf{q}, \omega) = i\langle [\mathcal{R}_{\mathbf{q}}(t), \mathcal{R}_{-\mathbf{q}}(0)] \rangle_{\omega}$ . This quantity can be conveniently expressed via the pseudospin susceptibility tensor  $\chi_{\alpha\beta}(\mathbf{q}, \omega) = i\langle [S_{\mathbf{q}}^{\alpha}(t), S_{-\mathbf{q}}^{\beta}(0)] \rangle_{\omega}$  calculated either by exact diagonalization (ED) on small clusters (see Appendix B for details) or within the linear spin-wave (LSW) approximation. For the geometry shown in Fig. 1(b), the RIXS intensity is roughly proportional to  $\frac{1}{2}(\chi''_{xx} + \chi''_{yy}) + \chi''_{zz}$  (neglecting the small off-diagonal contribution and summing up the  $\pi - \pi'$  and  $\pi - \sigma'$  scattering channels to account for the unpolarized detection).

## C. Identification of relevant parameter regime

To narrow down the parameter regime consistent with the experimental data, we perform a systematic scan through the parameter space of the model, inspecting the type of the magnetic order and the excitation spectra obtained by ED. As the six parameters present in the

model make this scan a challenging task, we use fixed small values of the subsidiary interactions ( $\Gamma'$  and  $J_{2,3}$ ) and vary only the main ones ( $J$ ,  $K$ , and  $\Gamma$ ). This limitation is not severe, since the overall dispersion and intensity distribution in the calculated RIXS spectra is determined by the dominant interactions, while the smaller ones affect only finer details of the spin dynamics not resolved in the experiment. Despite that, the  $\Gamma'$  and  $J_{2,3}$  interactions still play important roles in stabilizing the zigzag phase and extending it to the regime where the dominant interactions can reproduce the RIXS data.

The phase diagram focusing on the zigzag phase is presented in Fig. 3. To construct it, we assume small  $\Gamma' < 0$  associated with the trigonal compression [50] that is fixed at  $\Gamma' = -0.1A$  with  $A$  being the overall energy scale of the dominant interactions defined as  $A = \sqrt{J^2 + K^2 + \Gamma^2}$ . Similarly, the further-neighbor interactions  $J_2$  and  $J_3$  are fixed at  $J_2 = 0.05A$  and  $J_3 = 0.1A$ , respectively, putting thus more emphasis on the third-neighbor interaction as suggested by *ab initio* estimates [17]. The main interactions are parametrized using two angles  $\theta$ ,  $\phi$  as  $(J, K, \Gamma) = (A \sin \theta \cos \phi, A \sin \theta \sin \phi, A \cos \theta)$  with the ranges  $\theta \in [0, \pi/2]$  and  $\phi \in [0, 2\pi]$  covering the entire  $JK\Gamma$  parameter space with  $\Gamma > 0$ . The resulting phase diagram in Fig. 3 shows two zigzag regions connected by a narrow “neck” which substantially differ in the direction of the ordered moments. Let us consider for concreteness one of the degenerate zigzag patterns with zigzag chains running along the  $x$  and  $y$  bonds shown in Fig. 1(b). The ordered moments in the upper zigzag phase are then found close to the  $z$  axis, while the lower zigzag phase is characterized by the moment direction pointing roughly in between the  $x$  and  $y$  axes. These observations can be understood using simple energy-based arguments when comparing Fig. 1(b) and Eq. (1). The zigzag order of the upper phase found for  $K > 0$  and  $J < 0$  fully satisfies the AFM  $K$  interaction on the  $z$  bonds, where it picks up the dominant  $z$  component of the ordered moments as seen in Eq. (1). The energy gain from the remaining  $x$  and  $y$  bonds is due to FM  $J$  interaction. In the bottom zigzag phase covering mainly the  $K < 0$  and  $\Gamma > 0$  case, the FM Kitaev interaction profits from the FM bonds within the chains by using the  $x$  and  $y$  components of the pseudospins separately. The positive  $\Gamma$  interaction brings energy gain on the AFM interchain  $z$  bonds by utilizing the simultaneous presence of the  $x$  and  $y$  components. This phase is also significantly supported by the negative  $\Gamma'$  interaction (see Ref. [54] for a more detailed discussion). The longer-range AFM interactions  $J_2$  and particularly  $J_3$  further stabilize the zigzag state—now independently on the moment direction due to their isotropic character—and expand significantly the zigzag phases in the parameter space.

The experimentally determined direction of the ordered moments as given by Ref. [15] is consistent with the bottom zigzag region. Using the precise ordered moment direction

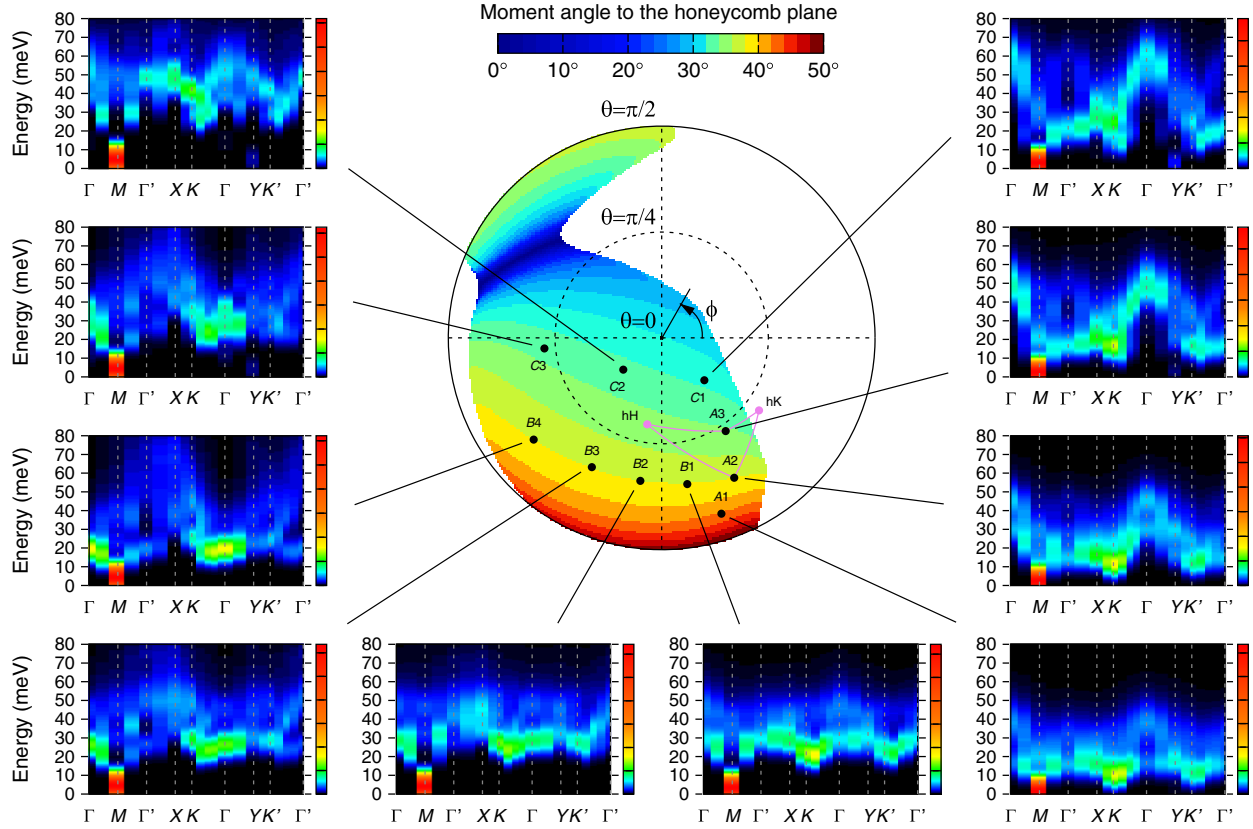


FIG. 3. Zigzag phase in the phase diagram of the extended Kitaev-Heisenberg model with the main interactions parametrized using the radial coordinate  $\theta$  and the azimuth  $\phi$  as  $J = A \sin \theta \cos \phi$ ,  $K = A \sin \theta \sin \phi$ ,  $\Gamma = A \cos \theta$ , and the smaller interactions kept constant:  $\Gamma' = -0.1A$ ,  $J_2 = 0.05A$ , and  $J_3 = 0.1A$ . Here,  $A$  is the overall energy scale, which is irrelevant for the phase diagram but determines the characteristic energies of the magnetic excitations. The color indicates the angle of the zigzag-ordered moments to the honeycomb plane. The data are obtained using the exact-diagonalization-based method in Ref. [51]. Small panels around the phase diagram show, for selected parameter points, the theoretical RIXS intensity maps calculated by exact diagonalization of the extended Kitaev-Heisenberg model on 24- and 32-site clusters (see Appendix B for details). We assume the scattering geometry depicted in Fig. 1(a) and present a sum of  $\pi - \pi'$  and  $\pi - \sigma'$  scattering channels (imitating an unpolarized detection) plotted along the same path through the Brillouin zone as in Fig. 1. The energies are determined by taking the value  $A = 29$  meV giving the best match between the A2 parameter point and the experimental data. Gaussian broadening with a FWHM of 25 meV is applied to the spectra. Finally, the violet lines show the pathways in the parameter space connecting the selected points A2 and A3 with the points of hidden symmetry utilized in Sec. III D 2. They should be understood as projections only, since the hidden Heisenberg point (hH) has  $\Gamma' \approx -0.4A$ , whereas the hidden Kitaev point (hK) has  $\Gamma' \approx -0.3A$ , and  $J_{2,3} = 0$  for both points.

as a very sensitive probe of the anisotropic exchange interactions, a further refinement of the relevant parameter regime is possible. Namely, we can utilize the angle of the ordered moments to the honeycomb plane which is estimated in a subsequent analysis of the experimental data in Ref. [15] to be around  $38^\circ$ – $40^\circ$  [51]. The theoretical values of this angle obtained by ED through the zigzag phase are indicated in Fig. 3. Considering solely the experimental moment direction, the matching parameter sets form a strip near the A2 and B1–B4 points in Fig. 3.

Let us now focus on the phase diagram in Fig. 3 from the point of view of our RIXS data. We calculate RIXS maps via ED for several selected parameter points assuming the same scattering geometry as in the experiment. Because of the finite size of the clusters used in ED, their ground states

entering the calculation of the dynamic response comprise all possible zigzag patterns in an equal-weight superposition. This mixing actually imitates the experimental conditions, since below  $T_N$  the long-range zigzag order in the sample is, in fact, accompanied by short-range zigzag orders with the complementary directions of the zigzag chains [15]. The maps, presented in Fig. 3, can thus be directly compared to the data in Fig. 1(d) up to the energy scale that is flexible by tuning  $A$ . Within the bottom zigzag phase, which covers a broad range of parameters, several kinds of spin-excitation behavior can be observed. The differences concern the wave vectors away from the  $M$  point that universally hosts an intense low-energy magnon through the whole zigzag phase.

In the left part of the phase diagram with significant negative  $J$  (representative B4 and C3 points), the overall

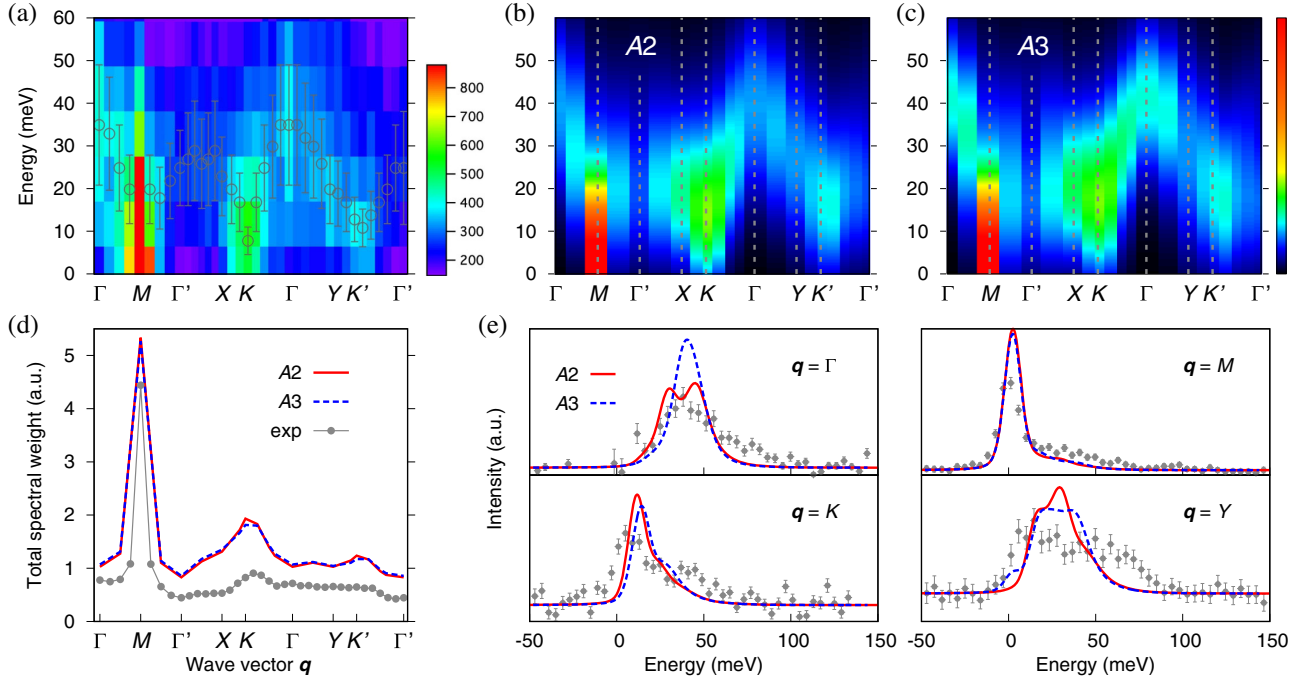


FIG. 4. (a) Experimental RIXS intensity map for  $T = 7$  K with the positions of the intensity maxima for the individual wave vectors indicated as open circles. (b) Theoretical RIXS intensity map calculated for the parameter values corresponding to the A2 point in Fig. 3 and the energy scale  $A = 29$  meV, which gives  $J \approx 12$  meV,  $K \approx -24$  meV,  $\Gamma \approx 11$  meV,  $\Gamma' \approx -3$  meV,  $J_2 \approx 1.5$  meV, and  $J_3 \approx 3$  meV. The scattering geometry depicted in Fig. 1(a) is assumed, and a sum of  $\pi - \pi'$  and  $\pi - \sigma'$  scattering channels is taken, corresponding to an unpolarized detection. The spectra are broadened in energy by Gaussians with a FWHM of 25 meV to imitate the experimental resolution as in (a). (c) The same as in (b) but for the parameter values corresponding to the A3 point in Fig. 3 and the energy scale of  $A = 24$  meV:  $J \approx 10$  meV,  $K \approx -15$  meV,  $\Gamma \approx 16$  meV,  $\Gamma' = -2.4$  meV,  $J_2 = 1.2$  meV, and  $J_3 = 2.4$  meV. (d) Energy-integrated RIXS response (total spectral weight) corresponding to (a)–(c). The experimental data, obtained by integrating in the  $[-30, 60]$  meV range, are arbitrarily scaled with respect to theoretical ones. (e) RIXS intensity profiles at selected wave vectors. High-resolution experimental data (gray dots) are compared to theoretical spectra for the above parameters (red and blue lines). The theoretical spectra are broadened by the experimental resolution function of the high-resolution setup.

shape of the intensity cloud hints to the proximity of the FM phase. There are intense low-energy excitations around the  $\Gamma$  point whose dispersion goes up toward the AFM wave vector  $\Gamma'$ —such features are shared with FM magnons. In the bottom part, one can notice a shift to the magnon breakdown regime reported for  $\alpha$ - $\text{RuCl}_3$  by Ref. [32] (representative  $B3$ ,  $B2$ , and  $B1$  points). It is most apparent near the  $J = 0$  line ( $B1$  and  $B2$  points), which shows a rather flat dispersion of excitations with a pronounced high-energy tail. Yet more incoherent scattering is seen at Kitaev-dominant point  $A1$ . The most robust features of the experimental RIXS spectra in Fig. 1(d) are the dispersing excitations in the  $K$ - $\Gamma$ - $Y$ - $K'$  part, reaching the maximum energy at the  $\Gamma$  point and maximum intensity at the  $K$  point. This feature can be clearly observed in the theoretical maps on the right corresponding to the parameter points with a sizable AFM  $J > 0$  ( $C1$ ,  $A3$ , and  $A2$  points). A hint of this feature is displayed also at the  $A1$  and  $C2$  points of the highly dominant  $\Gamma$  interaction and FM  $J < 0$ . In the  $C2$  case, the intensity resides at relatively high energies, being connected to the  $M$ -point magnons by a steep excitation branch.

Taking into account also the experimental constraint on the ordered moment angle to the honeycomb plane, the suggested parameter range for  $\text{Na}_2\text{IrO}_3$  lies around points  $A2$  and  $A3$  in Fig. 3, i.e., in the regime with  $\Gamma$  comparable to or somewhat less than  $|K|$  and quite sizable AFM  $J > 0$ . For the  $A2$  point, the moment angle to the honeycomb plane fits well the experimental value; the  $A3$  point may seem to match slightly better the experimental RIXS map. In the following, we thus discuss both these points in parallel to give a broader picture of the relevant parameter range.

To enable a one-to-one comparison, Figs. 4(b) and 4(c) present the theoretical RIXS spectra for the  $A2$  and  $A3$  points, respectively, with the resolution matching the experimental one and with the values of the energy scale  $A$  tuned to fit the position of the main peak at the  $q = 0$  wave vector ( $\Gamma$  point). Figure 4(a) shows the experimental RIXS intensity map for  $T = 7$  K with the positions of the intensity maxima for the individual wave vectors indicated as open circles, where the specular elastic scattering peaks at  $\Gamma$  and  $\Gamma'$  are subtracted. The broad maps in Figs. 4(a)–4(c) show a good overall agreement of the theoretical maps with the RIXS data in both the dispersion

and intensity distribution in the Brillouin zone. The latter is supported by the total spectral weight (energy-integrated spectra) in Fig. 4(d), which seems to match quite well to the corresponding experimental data in Fig. 1(f). Here, essentially no difference between  $A2$  and  $A3$  points is observed.

Figure 4(e) compares the high-resolution experimental RIXS spectra in Fig. 2(a) to the theoretical spectra convoluted with the experimental resolution function. The main incoherent and coherent features of the  $\Gamma$  and  $K$  spectra are well captured by the theoretical spectra. A discrepancy is that the theoretical spectra show relatively less spectral weight in high-energy parts. At the  $M$  point, the incoherent high-energy part is reasonably reproduced by the model. At the  $Y$  point, the discrepancy in the incoherent high-energy intensity seems bigger. Overall, the theoretical spectra clearly capture the main features of the spectra at the individual wave vectors including, to some extent, also the shape of intensity profiles following the central peaks.

Since the data for the various cluster sizes and shapes seem to be quite consistent in the energy ranges and profiles of the modes, we cannot attribute the discrepancy in the incoherent high-energy parts solely to finite-size effects. Even though the extended Kitaev-Heisenberg model captures the essential dynamics of the  $J_{\text{eff}} = 1/2$  pseudospins, it may lack certain scattering processes that lead to the enhancement of the high-energy tails. One such mechanism may be a magnetoelastic coupling that comes into play due to the large orbital component of the  $J_{\text{eff}} = 1/2$  pseudospins and may act as an additional decay channel. Pronounced effects of coupled lattice and pseudospin dynamics are observed, for example, in phonon line shapes in Raman spectra of perovskite iridates [55,56]. Reference [43] introduces the phonon contributions as producing a series of harmonic peaks to describe the incoherent high-energy scatterings. Few facts, however, suggest that there are no big direct phonon contributions to the incoherent high-energy parts. It is known that the resonant phonon contribution becomes visible when the inverse core-hole lifetime is in the range of a few hundred meV, and a 1 eV detuning of the lifetime leads to a near-zero cross section [57]. At the Ir  $L_3$ , the inverse core-hole lifetime is more than 5 eV [58], and this shorter-lived core hole state is not expected to provide sufficient time for the lattice to respond. A majority of optical phonon modes of  $\text{Na}_2\text{IrO}_3$  and  $\text{Li}_2\text{IrO}_3$  reside around 60 meV [59]. Recent O  $K$ -edge RIXS on  $\text{Li}_2\text{IrO}_3$  report the resonant phonon spectra where the fundamental phonon is at 70 meV [60]. The Ir  $L_3$ -edge RIXS on  $\text{Li}_2\text{IrO}_3$  [44], on the other hand, shows that the low-energy excitation feature is centered at 20 meV, which is notably lower than 70 meV and so of a different origin from phonon. Our high-resolution spectra in Fig. 4(e) do not show maximum intensities at this energy range but show decreasing intensities, for example, at  $\Gamma$ ,  $K$ , and  $M$ . As mentioned earlier, Ref. [44] argues against the phonon interpretation by showing that the energy scale of

the incoherent feature is very different in two isostructural  $\text{Na}_2\text{IrO}_3$  and  $\text{Li}_2\text{IrO}_3$ . Hence, we assign the incoherent high-energy scattering as of magnetic origin.

The x-ray and neutron diffraction studies [11,13,14] show that there are inherent imperfections in crystal structure such as stacking faults and site disorders, which result in a structural diffuse scattering and a remaining short-range order below the ordering temperature [13,15]. Small variations in the structure can alter various exchange interactions in  $\text{Na}_2\text{IrO}_3$ . So it is possible that the current single parameter set should be supplemented with nearby parameter sets among many in Fig. 3 to explain the discrepancy in the incoherent high-energy parts and fully reproduce the whole observed spectra.

#### D. Nature of the spin excitations

Having the main magnetic intensity in the RIXS spectra below approximately 60 meV reasonably well captured by the excitations of the extended Kitaev-Heisenberg model, it is natural to ask what the character is of those excitations. In the following, we address this issue by comparing ED results to the linear spin-wave approximation and by inspecting the evolution of the spectra when moving in the parameter space toward points of hidden symmetry. In the latter case, we use a nearby hidden Heisenberg point where a magnon picture is valid and a nearby hidden Kitaev point with the excitations carried by Majorana fermions.

##### 1. Comparison to linear spin-wave approximation

Each of Figs. 5(a) and 5(b) presents fine energy-resolved RIXS spectra obtained by ED and LSW calculation for the  $A2$  and  $A3$  points, respectively, used also in Figs. 4(b) and 4(c). In the case of the  $A3$  point with  $\Gamma \approx |K|$  shown in Fig. 5(b), the LSW approximation seems quite successful in capturing the overall dispersion and intensity of the spin excitations, the main difference being the high-energy magnon branches that get significantly renormalized in terms of both the energy shift and broadening. Figure 5(d) shows that the distributions of the total spectral weight are in excellent agreement between ED and LSW. In the case of the  $A2$  point with  $\Gamma \approx \frac{1}{2}|K|$  shown in Fig. 5(a), the agreement is spoiled by the fact that LSW places this parameter point closer to a competing order with the characteristic wave vector  $K$ . The reason is that the minimization of purely classical energy in the LSW approximation completely neglects quantum fluctuations supporting the zigzag phase. As a consequence, LSW brings down the excitations at both  $K$  and  $K'$  and lifts the  $M$ -point magnon. There is also an associated shift of the spectral weight from the  $M$  point to the  $K$  and  $K'$  points as shown in Fig. 5(c). This result is in contrast to the ED calculations, which give similar low-energy spectra for both  $A2$  and  $A3$  points. However, apart from these trends related to a phase boundary shift, the LSW description of the  $A2$  point successfully gives a rough picture

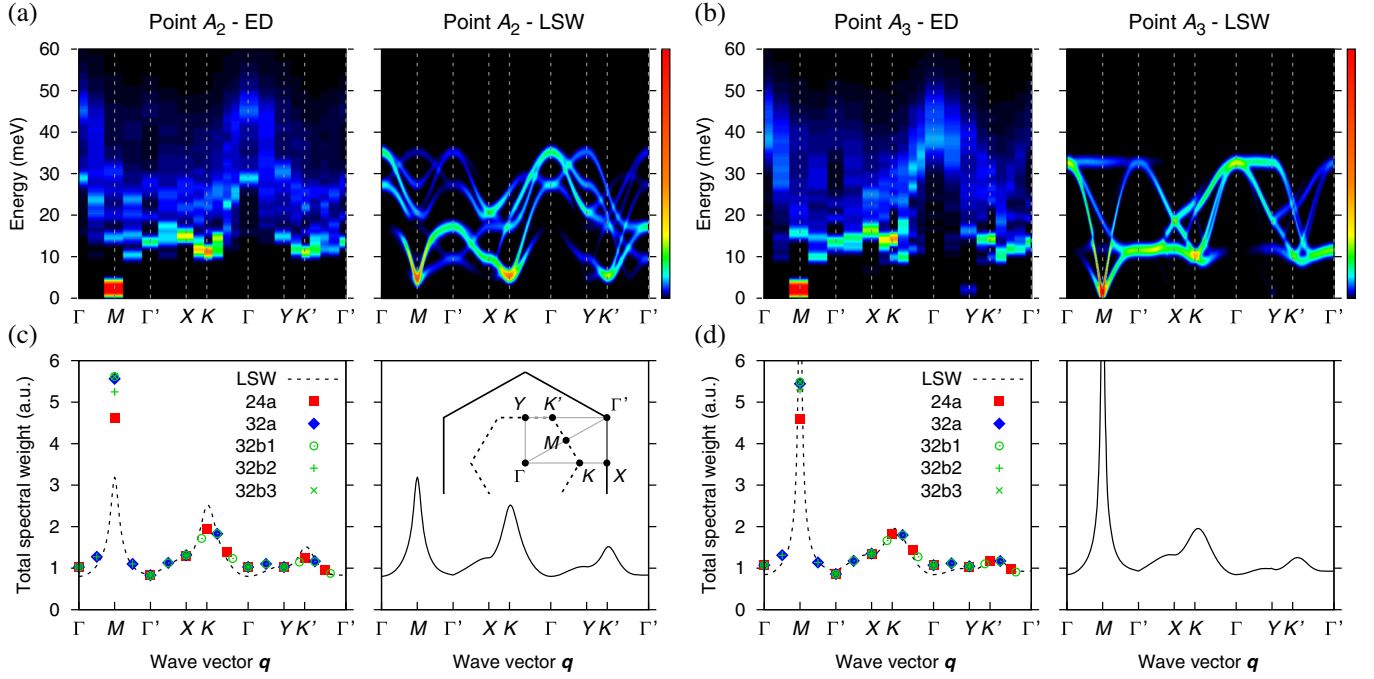


FIG. 5. (a) RIXS intensity maps for the parameter point  $A_2$  and the same energy scale as in Fig. 4(b). The left and right are obtained by exact diagonalization and the linear spin-wave approach, respectively. To better resolve the finer features, Gaussian broadening with a small FWHM of only 2 meV is used in both cases. In the case of LSW, the spectra are averaged by equally employing all three possible zigzag pattern directions. This procedure leads to a map that could be directly compared to the ED one, since the cluster ground state used in ED contains all zigzag pattern in an equal-weight superposition. (b) The same for the parameter point  $A_3$  and the energy scale as in Fig. 4(c). (c) Energy-integrated RIXS response (total spectral weight) corresponding to (a). Data for all the clusters are presented, showing negligible finite-size effects on the spectral weight. The curve obtained by the linear spin-wave approach (right) is shown also on the left by a dashed line. (d) Total spectral weight for the data in (b).

of the excitation branches. The high-energy branches at the  $\Gamma$  point are now visibly split. According to the LSW calculation, the lower branch corresponds to oscillations of the moment angle to the honeycomb plane and the upper one to the oscillations in the in-plane direction perpendicular to the zigzag chains.

Based on the above results, it seems quite likely that the spin-excitation spectra could be reproduced when going beyond LSW and include the anharmonic effects, e.g., by correcting the dispersions via the self-consistent spin-wave theory and by implementing finite magnon lifetimes due to magnon decay processes [31]. An attempt to evaluate the magnon decay in a Kitaev system, utilizing the so-called imaginary self-consistent Dyson equation approach, was recently performed by Winter *et al.* [32] when interpreting the neutron data on  $\alpha$ - $\text{RuCl}_3$ . Note that in their case the multimagnon contribution seems stronger (Fig. 6 in Ref. [32]) due to a different parameter regime within the zigzag phase.

## 2. Proximate hidden Kitaev and Heisenberg points

The applicability of the magnon picture can be further checked by inspecting the evolution of the calculated RIXS spectra when going through the parameter space toward

suitable reference points. The parameter region identified as relevant for  $\text{Na}_2\text{IrO}_3$  lies close to two of the points of special symmetry [61], where the nearest-neighbor extended Kitaev-Heisenberg model can be exactly mapped to either the Kitaev or Heisenberg model. Since in both the pure Kitaev and Heisenberg cases the spin excitations are well known, the special-symmetry points provide convenient references for us. In the following, we keep the discussion of both special-symmetry points very brief; further details can be found in Appendix C or the original Ref. [61].

Working in the representation utilizing the energy scale  $A$ , our point  $A_2$  corresponds to

$$(J, K, \Gamma, \Gamma')_{A_2} \approx (0.4, -0.8, 0.4, -0.1)A \quad (4)$$

complemented by the small  $J_{2,3}$ . Similarly, for the  $A_3$  point, we have

$$(J, K, \Gamma, \Gamma')_{A_3} \approx (0.4, -0.6, 0.7, -0.1)A. \quad (5)$$

The hidden Kitaev point is obtained for the parameter set

$$(J, K, \Gamma, \Gamma')_{\text{hK}} \approx (0.6, -0.5, 0.6, -0.3)A, \quad (6)$$

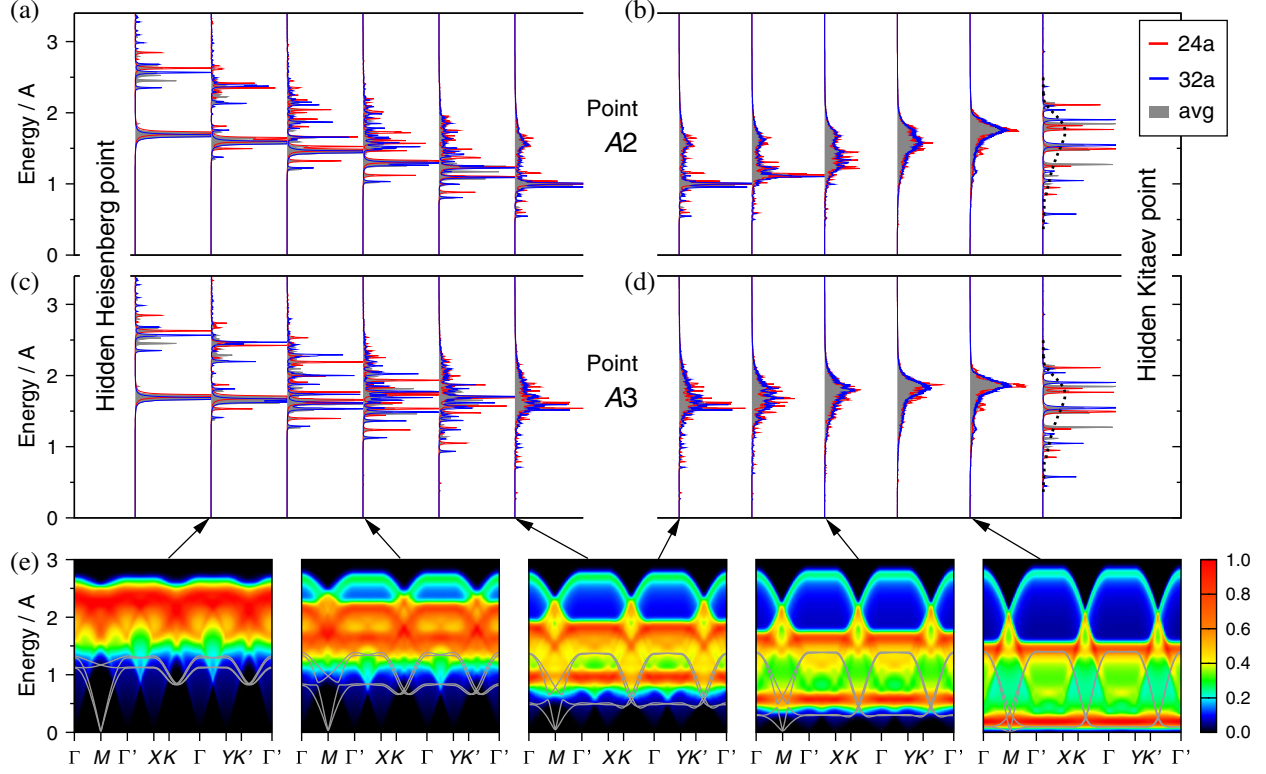


FIG. 6. (a) Evolution of the theoretical  $\Gamma$ -point ( $\mathbf{q} = 0$ ) RIXS intensity on a line through the parameter space going from the hidden Heisenberg point  $(J, K, \Gamma, \Gamma') \approx (-0.1, -0.6, 0.8, -0.4)A$  to the point A2 of Fig. 3. The line lies completely in the zigzag phase. Finite-size effects can be estimated by comparing data for various clusters shown in Appendix B. The average is taken over all of them (i.e., 24a, 32a, and 32b1 to 32b3). The spectra are presented in units of the energy scale  $A$  and only a tiny broadening is used to resolve the structure of the continuum. (b) The same for a line connecting the point A2 and the hidden Kitaev point  $(J, K, \Gamma, \Gamma') \approx (0.6, -0.5, 0.6, -0.3)A$ . Apart from the last point, the ground state remains zigzag ordered. The dotted line indicates scaled exact solution in the AFM Kitaev limit [63]. (c,d) Same as panels (a,b) but for the A3 point of Fig. 3. (e) Two-magnon density of states for selected points of panels (c) and (d) calculated using the linear spin-wave dispersions (gray lines). Single zigzag pattern of Fig. 1(b) was assumed, its Bragg spots correspond to the  $Y$  points.

where  $J_2$  and  $J_3$  are zeros as the longer-range interactions are absent at this special-symmetry point. It may be derived by taking the canonical Kitaev model and rotating the interaction axes  $x$ ,  $y$ , and  $z$  by  $180^\circ$  around the axis perpendicular to the honeycomb plane (see Appendix C for a detailed discussion). This way, we arrive at the extended Kitaev-Heisenberg model with the above parameter set. Since the transformation is exact, all the features including, e.g., the fermionic excitation spectrum, are exactly preserved. At the hidden Kitaev point, we thus find the behavior of the extended Kitaev-Heisenberg model to be identical to the Kitaev model with interaction parameter  $K_0 \approx 1.4A$ , up to a simple global rotation. At the second considered hidden-symmetry point with the parameter set

$$(J, K, \Gamma, \Gamma')_{\text{hH}} \approx (-0.1, -0.6, 0.8, -0.4)A, \quad (7)$$

the extended Kitaev-Heisenberg model exactly maps to the Heisenberg model with the interaction constant  $J_0 \approx 0.9A$ . In this case, the derivation is more complicated and

includes a four-sublattice transformation connecting zigzag and Néel order (cf. Refs. [61,62] and Appendix C). The spin-excitation spectra are then directly linked to those of the simple Heisenberg antiferromagnet on the honeycomb lattice, but a momentum shift by  $\mathbf{q} = M$  and equivalent wave vectors is involved.

Figure 6 presents the parameter evolution of the RIXS response, focusing on the  $\Gamma$ -point ( $\mathbf{q} = 0$ ) intensity containing the prominent high-energy feature that is a signature of the lack of the global rotational symmetry of the model. The model parameter sets are linearly interpolated between the A2 and A3 points and the hidden-symmetry points, all given by Eqs. (4)–(7). Note that the latter parameter points differ essentially in  $J$  only while having roughly the same  $\Gamma/|K|$  ratio as our A3 point and an enhanced negative value of  $\Gamma'$  compared to A2 and A3. An explicit plot of the parameters used in Fig. 6 can be found in Appendix C, and the corresponding pathways are indicated in the overall phase diagram in Fig. 3 in a projected form (note that  $\Gamma'$  and  $J_{2,3}$  change once we depart from the A2 and A3 points).

The evolution from the hidden Heisenberg point toward the A2 and A3 points shown in Figs. 6(a) and 6(c), respectively, starts with a simple response profile containing a sharp magnon peak and a two-magnon continuum characteristic for the Heisenberg model. The magnon at the  $\Gamma$  point calculated for the zigzag phase is, in fact, a copy of the Néel AFM magnon at the  $M$  point shifted by means of the hidden-symmetry transformation. Therefore, it appears at a high energy ( $\sqrt{2}J_0$  in the LSW approximation). Going away from the hidden Heisenberg point, the high-energy magnon branches get broadened via magnon scattering and slowly merge with the two-magnon continuum forming the broad high-energy features observed at our points. The gradual onset of the magnon scattering is further illustrated in Fig. 6(e) by comparing the LSW dispersions and the two-magnon density of states (DOS):  $\mathcal{D}_2(\omega) = \sum_{nq, n'q'} \delta(\omega - \omega_{nq} - \omega_{n'q'})$ , where  $\omega_{nq}$  stands for the dispersion of the  $n$ th magnon branch. Neglecting the magnon-magnon interaction vertex, this quantity indicates the strength of the scattering continuum accessible when keeping the kinematic constraint [31]. It becomes gradually activated as we depart from the hidden Heisenberg point, where the two-magnon decay does not occur and the basic decay channel involves three-magnon processes [31,32].

Continuing further from our points to the hidden Kitaev point, Figs. 6(b) and 6(d) show that the zigzag order is maintained almost up to the hidden Kitaev point. This result is natural, since the hidden KQSL comes with an anti-ferromagnetic effective Kitaev interaction. As revealed by the study of the Kitaev-Heisenberg model [62], the AFM KQSL phase has a limited extent compared to the FM KQSL phase because of a stronger competition with the surrounding phases that gain energy due to quantum fluctuations [64]. The high-energy continuum in the  $\Gamma$ -point response is present up to the zigzag to KQSL boundary with moderate changes in its shape that seem to be correlated with the two-magnon DOS. Upon entering the KQSL, there is an abrupt change in the character of the spectrum that later only negligibly evolves when approaching the exact hidden AFM Kitaev point as shown in Figs. 6(b) and 6(d). The continuum spreads over a larger spectral range and becomes composed of sharp peaks reflecting the excitations being carried by (almost) non-interacting Majorana fermions with a set of possible momenta strongly limited by the cluster. Nevertheless, the overall distribution of the spectral weight can be successfully compared to the exact result for an infinite lattice [63].

The above observations suggest that the picture of renormalized magnons adequately captures the spin excitations within the extended Kitaev-Heisenberg model in the parameter regime matching the low-temperature RIXS data below  $\lesssim 60$  meV. This suggestion is supported by the good overall agreement of LSW dispersions, intensity, and spectral weight distribution in the Brillouin zone with

the ED results. Moreover, the magnon broadening seems to correlate well with the two-magnon DOS that gives hints about the decay rates of the individual magnon branches. Compared to the recent analysis of spin excitations in  $\alpha$ -RuCl<sub>3</sub> [32] that placed  $\alpha$ -RuCl<sub>3</sub> to the regime of magnon “breakdown” within the same spin model as used here, we encounter better-defined magnons with a less extended background of the multimagnon character.

Despite the relative proximity of the KQSL associated with the hidden Kitaev point, in particular, for the A3 point, the model spectra for zero temperature do not clearly bear the features characteristic for the Kitaev limit, most importantly, the flat dispersions of the spin excitations that are seen in the exact results for the Kitaev model [63,65] or the study of its perturbed variant [66]. An interesting result in this context is the recent finding by Gohlke *et al.* [20] that the  $K$ - $\Gamma$ -only model shows signatures of a spin-liquid ground state in a wide parameter range. A later study by Wang, Normand, and Liu [67] using the variational quantum Monte Carlo method revisits those results and finds a proximate Kitaev spin liquid with a different structure than KQSL for negative  $K$  and  $\Gamma/|K|$  up to roughly 0.6. In the parameter area that we identify as relevant for Na<sub>2</sub>IrO<sub>3</sub>, the large  $K$  and  $\Gamma$  are complemented by sizable  $J$  and a number of smaller interactions; nevertheless, the spin dynamics within the  $K$ - $\Gamma$ -only model and a possible connection to our case is a highly relevant problem.

## IV. MAGNETIC EXCITATION SPECTRA AT A HIGH TEMPERATURE

### A. Temperature evolution of magnetic excitation spectra

A defining feature of quantum spin liquids is an emergent magnetic excitation carrying fractional quantum numbers. In the case of KQSL, the fractionalized magnetic excitations are represented by Majorana fermions [1–3]. When a conventional magnetic order is thermally melted, a signature of QSL may be found in the spin dynamics over a wide temperature range. A recent INS study of  $\alpha$ -RuCl<sub>3</sub> reports a highly unusual temperature-stable signal around the zone center, which is interpreted as a dynamical response of the Majorana fermions of the KQSL due to thermal fluctuations of fluxes [27–30,35,68]. The recent RIXS work [44] on Na<sub>2</sub>IrO<sub>3</sub> suggests that the dynamical spin-spin correlation of the broad scattering is restricted to nearest neighbors and phenomenologically similar to the unusual broad INS scattering of  $\alpha$ -RuCl<sub>3</sub>. In Fig. 2(d), the broad scattering at the  $K$  point is presented to survive up to 150 K, showing that Na<sub>2</sub>IrO<sub>3</sub> also has a highly unusual temperature-stable signal. In this section, we present the temperature evolution of the RIXS spectra over the full Brillouin zone up to 280 K to show the thermal characteristics of dynamic spin correlations in a paramagnetic phase of Na<sub>2</sub>IrO<sub>3</sub>.

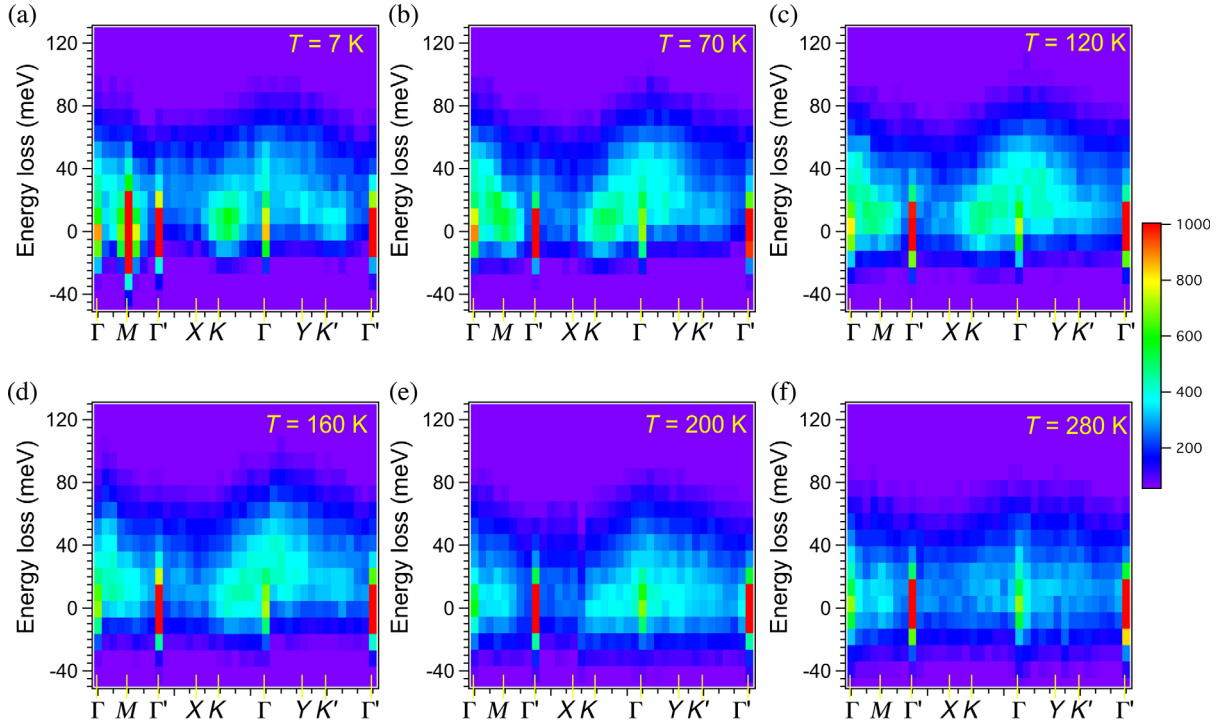


FIG. 7. Temperature evolution of magnetic excitation spectra. (a)  $T = 7$  K. (b)  $T = 70$  K. The magnetic Bragg peak at the  $M$  disappears, indicating disappearing zigzag correlations. Spectral intensities fill in between  $\Gamma$  and all first Brillouin zone symmetric points ( $M$ ,  $K$ ,  $K'$ , and  $Y$ ), connecting the high-energy feature at the  $\Gamma$  to the low-energy features at the  $M$ ,  $K$ , and  $Y$ . This trend becomes more pronounced at (c)  $T = 120$  K and (d)  $T = 160$  K. (e)  $T = 200$  K. Spectral intensities move toward lower energy. (f)  $T = 280$  K. The RIXS intensity over the whole Brillouin zone substantially diminishes.

Figure 7(b) shows an intensity color map of RIXS spectra at  $T = 70$  K. The specular elastic peaks at  $\Gamma$  and  $\Gamma'$  are seen as in the  $T = 7$  K map in Fig. 7(a). Because the short-range zigzag order disappears at this temperature, the magnetic Bragg peak at the  $M$  point is largely suppressed, exposing an underneath low-energy excitation [15]. The low-energy excitation at the  $K$ ,  $Y$ , and  $K'$  and the high-energy excitation at the  $\Gamma$  stay more or less the same at  $T = 70$  K. On the other hand, it is seen that the spectral intensity near the  $\Gamma$  point unusually grows up at  $T = 70$  K, connecting the high-energy excitation at the  $\Gamma$  to the low-energy excitations at the  $M$ ,  $K$ ,  $Y$ , and  $K'$  points. This temperature evolution of the spectral intensity distribution becomes more pronounced up to  $T = 160$  K as shown in Figs. 7(c) and 7(d).

Noticeable changes are observed at  $T = 200$  K. The overall RIXS scattering intensity becomes weakened and moves toward lower energy, confining its significant weight within 60 meV as shown in Fig. 7(e). The scattering intensity displays a triangular shape along the  $K$ - $\Gamma$ - $Y$ - $K'$  path. At  $T = 280$  K, the RIXS scattering intensity over the whole Brillouin zone substantially diminishes, resulting in a featureless spectrum as in a paramagnet as shown in Fig. 7(f). The weakening RIXS intensity at a high temperature is at odds with the Ref. [43] RIXS work but consistent with Ref. [44]. As discussed in Secs. II B and III C, it is not

necessary to invoke the lattice degrees of freedom to describe our spectra, and the observed excitations are assigned as of magnetic origin.

In a two-dimensional system, short-ranged spin correlations above the long-range order temperature are visible as a diffusive scattering at the vicinity of characteristic points in the Brillouin zone. As the temperature increases further, the short-range order dies and the corresponding spectral weight disappears. Seemingly, the temperature dependencies of the low-energy spectral weights around the  $M$  and  $K$  points follow this general tendency. However, the observed intensity modulations in other areas than the  $K$  and  $M$  are unusual. In particular, this temperature-dependent intensity modulation is seen at a high energy, whose energy is beyond the thermal energy of room temperature. Magnetic excitations at intermediate temperatures are broad in energy and momentum and remind us of unusual scatterings over a large energy interval revealed in  $\alpha$ - $\text{RuCl}_3$  through the INS [27,29,30].

## B. Dynamic spin correlations in a paramagnetic phase

In this section, we discuss the observation that the spectral intensity in a large region surrounding the  $\Gamma$  point unusually grows up to 160 K, connecting the high-energy feature at the  $\Gamma$  point to the low-energy feature at the  $M$ ,  $K$ , and  $Y$  points and becomes a diffusive low-energy scattering

with negligible momentum dependence at 280 K (Fig. 7). As the ED calculations in Fig. 6 show, the broad feature below the ordering temperature contains the spontaneous magnon decay into a two-magnon continuum. Two-magnon excitations include pairs of very short wavelength spin waves and can remain at higher temperatures than single-magnon excitations. However, two-magnon scattering cannot explain the increasing spectral weights over the large Brillouin region, because the zigzag correlations decrease as the temperature increases as evidenced by decreasing intensities near the  $K$  and  $M$  points.

In a frustrated spin system above the ordering temperature, the larger interactions can keep short-range correlations up to quite high temperatures comparable to the energy scale of these interactions. The corresponding fragments of a few specifically correlated spins have a specific dynamics determined by the dominant interactions. In our case, the dynamics at elevated temperatures may be influenced by the proximity of hidden KQSL in the parameter space as well as the large scales of  $K$  and  $\Gamma$  that are suggestive of a possible connection to spin-liquid ground states in the  $K$ - $\Gamma$  model that are currently being investigated [20,67,69]. Reliable finite-temperature calculations of the dynamic response are challenging and out of the scope of the present ED scheme. Fortunately, a number of results exist for the integrable pure Kitaev model. An exact solution for spin dynamics at zero temperature is known [63,65], and detailed finite-temperature behaviors of the FM and AFM Kitaev systems are available from studies combining the cluster dynamical mean-field theory and the continuous-time quantum Monte Carlo method (CDMFT + CTQMC) [35,70]. Given the connections mentioned above, here we discuss our observations in the context of Kitaev systems at a finite temperature.

The thermal characteristics of Kitaev systems are understood in terms of fractionalization of spins  $\frac{1}{2}$  into itinerant Majorana fermions coupled to  $Z_2$  fluxes represented by localized Majorana fermions [1]. Two characteristic crossover temperatures appear [68]. At the lowest temperatures below  $T_L \approx 0.012$  K related to the  $Z_2$  flux gap, an almost flux-free state is found, with only low-energy itinerant Majorana fermions being thermally excited. Intermediate temperatures are characterized by thermally activated  $Z_2$  fluxes, but the itinerant Majorana fermions still retain their coherence. Finally, around  $T_H \approx 0.375$  K, the fluxes and Majorana fermions recombine into spins, the nearest-neighbor spin correlations decay, and the system is adiabatically connected to a conventional spin- $\frac{1}{2}$  paramagnet.

Much of this physics is discussed in the context of  $\alpha$ -RuCl<sub>3</sub>. The successive thermal fractionalization finds its thermodynamic signatures in magnetic specific heat data in  $\alpha$ -RuCl<sub>3</sub> where two separated broad peaks exist and a plateau in between two peaks is pinned at half of the ideal  $R \ln 2$  magnetic entropy [30,35,70]. Raman scattering observes a polarization-independent broad continuum [33]

successfully interpreted as due to pairs of itinerant Majorana fermions [34]. Banerjee *et al.* report a highly unusual scattering in  $\alpha$ -RuCl<sub>3</sub> through the INS which is broad in energy and momentum and remains at a high temperature, stimulating much research directed at identifying unique dynamic correlations of emergent Majorana fermions in systems close to KQSL [27,29]. Theoretical works indicate that the characteristic broad scattering of the KQSL is preserved in a proximate phase with long-range ordered spins (proximate KQSL) [37]. The proximate KQSL picture has been further elaborated experimentally and theoretically to understand the finite-temperature behavior [30,35,65,70].

Similarly to  $\alpha$ -RuCl<sub>3</sub>, Na<sub>2</sub>IrO<sub>3</sub> shows properties in the paramagnetic phase that can be interpreted as arising from the fractionalization to Majorana fermions. The two separated broad maxima in magnetic specific heat are also present in Na<sub>2</sub>IrO<sub>3</sub> with one around 20 K and the other around 110 K [40]. Half of the ideal  $R \ln 2$  entropy is gained at around 60 K, and the full  $R \ln 2$  entropy is recovered at more than 150 K, whose behavior is in good agreement with theoretical predictions [68,71]. Signatures of Kitaev-like correlations are seen in Raman scattering [38]. In this work, we measure the low-energy RIXS response, which, adopting the fast-collision approximation, is closely related to the dynamic structure factor by the INS [52,72]. The momentum- and energy-resolved magnetic excitation spectra show that magnetic excitations in Na<sub>2</sub>IrO<sub>3</sub> are broad in energy and momentum at intermediate temperatures, reminding of the unusual scatterings over a large energy interval in INS on  $\alpha$ -RuCl<sub>3</sub> [27,29].

An apparent difference between Na<sub>2</sub>IrO<sub>3</sub> and  $\alpha$ -RuCl<sub>3</sub> is in the energy scales. Magnetic excitations in Na<sub>2</sub>IrO<sub>3</sub> are observed at a much higher energy than those in  $\alpha$ -RuCl<sub>3</sub> which are confined within the 15 meV energy window [27–30,43]. The broad excitation at the  $\Gamma$  point [Fig. 2(b)] locates at 36 meV, while the one in  $\alpha$ -RuCl<sub>3</sub> can be viewed as a diffusive quasielastic scattering. The short-ranged correlations of three spin domains carrying their own zigzags persist at a much higher temperature than in  $\alpha$ -RuCl<sub>3</sub> [15]. The attempts to quantify the interactions based on the INS data in  $\alpha$ -RuCl<sub>3</sub> produce  $(J, K) = (-4.6, 7)$  meV in the  $J$ - $K$  model,  $(K, \Gamma) = (-6.8, 9.5)$  meV in the  $K$ - $\Gamma$  model, and  $(J, K, \Gamma) = (-0.5, -5, 2.5)$  meV in the nearest-neighbor model Hamiltonian [27,28,32], while our analysis of the RIXS data in Na<sub>2</sub>IrO<sub>3</sub> gives larger values; for example, the A2 and A3 points correspond to  $(J, K, \Gamma) = (12, -24, 11)$  and  $(10, -15, 16)$  meV, respectively. Related to the discussion in terms of the Kitaev model, the hidden KQSL found near our fit point is driven by the effective Kitaev interaction of AFM type with the strength of about  $K_0 \approx 35$ –40 meV (see Appendix C), giving, e.g., the crossover temperature of  $T_H \approx 140$ –170 K.

In studies of  $\alpha$ -RuCl<sub>3</sub>, the temperature evolution of the broad scattering features is described by the isotropic

Kitaev model with an FM Kitaev interaction,  $K = -16.5$  meV [30]. The CDMFT + CTQMC calculation on the FM Kitaev system finds that a quasielastic response at zero energy is large around the  $\Gamma$  point at a low temperature and becomes diffusively broadened in energy at a high temperature, ending up in a conventional paramagnetic phase, which is consistent with the experimental observations by the INS [30,35,70]. On the other hand, the CDMFT + CTQMC calculation on the AFM Kitaev system shows that an incoherent flat feature at  $\omega \sim K_0$  is seen around the  $\Gamma$  point at a low temperature, while a quasielastic response is distributed on the Brillouin zone boundary [35,70]. As the temperature increases, the incoherent feature becomes diffusively broadened in energy and is connected to the quasielastic response on the Brillouin zone boundary, losing its flat dispersion. The incoherent broad feature at  $\omega \sim K_0$  merges to a diffusive response at zero energy when the AFM Kitaev system adiabatically enters into a conventional paramagnetic phase. These finite-temperature behaviors of the AFM Kitaev system bear a similarity to the observed temperature evolution of our magnetic excitation spectra. The spectral intensity in a large region surrounding the  $\Gamma$  unusually grows up to 160 K, connecting the high-energy feature at the  $\Gamma$  to the low-energy feature at the  $M$ ,  $K$ , and  $Y$  points as shown in Fig. 7. The overall spectral weight moves toward lower energy at 200 K and shows a diffusive response with negligible momentum dependence at 280 K.

## V. CONCLUSION AND OUTLOOK

In this study, magnetic excitation spectra in a honeycomb lattice  $\text{Na}_2\text{IrO}_3$  were obtained for the wide-range reciprocal space up to the second Brillouin zone using the RIXS spectrometer. The state-of-the-art 12 meV measurements could identify the low-energy sharp magnon peak below the AFM order temperature and verify the broad widths of magnetic excitations. These sets of data allow a detailed comparison with theoretical calculations. The dispersion and spectral intensity distribution in the reciprocal space of RIXS spectra are well reproduced by the simulation using the exact diagonalization method on finite-size clusters. The parameter regime is characterized by large  $K < 0$  and  $\Gamma > 0$  complemented by sizable  $J > 0$  with small  $J_2$  and  $J_3$ , and  $\Gamma' < 0$ . We examine two of the points of special symmetry, i.e., AFM Heisenberg and AFM Kitaev, close to the parameter region of  $\text{Na}_2\text{IrO}_3$  and investigate the evolution of the spin excitations along paths connecting the special-symmetry points and the parameter points of  $\text{Na}_2\text{IrO}_3$ . This inspection suggests that the main magnetic intensity below the ordering temperature can be reasonably explained by the picture of renormalized magnons.

Magnetic excitation spectra in  $\text{Na}_2\text{IrO}_3$  show unusual spectral intensity modulations in a large region surrounding the  $\Gamma$  point at elevated temperatures. Finite-temperature calculations of the complex spin Hamiltonian are

challenging and not available at the moment. We conjecture that the dominant nearest-neighbor interactions keep short-range correlations up to quite high temperatures with a specific short-range dynamics which has a possible connection to a proximate spin-liquid phase. An interesting experimental direction is given by a theoretical suggestion that the full continuum of the Majorana fermions of the KQSL can be mapped without interference with flux excitations using the spin-conserving scattering of the RIXS [72]. The spin-conserving measurements require two instrumental capabilities which cannot be achieved using a standard (spherical-analyzer-based) RIXS spectrometer: a high-energy resolution and an efficient scattered x-ray polarization analysis [73,74]. Recently, a new flat crystal RIXS analyzer system was developed, which provides a polarization analysis without compromising the energy resolution and with high efficiency [46]. If successful, the spin-conserving RIXS measurements will give a transparent description of the existence of a proximate KQSL in  $\text{Na}_2\text{IrO}_3$ .

## ACKNOWLEDGMENTS

The use of the Advanced Photon Source at the Argonne National Laboratory was supported by the U.S. Department of Energy under Contract No. DE-AC02-06CH11357. J. C. acknowledges support by Czech Science Foundation (GAČR) under Project No. 19-16937S and MŠMT ČR under NPU II Project No. CEITEC 2020(LQ1601). Computational resources were supplied by the Ministry of Education, Youth and Sports of the Czech Republic under the Project CERIT-Scientific Cloud (Project No. LM2015085) provided within the program Projects of Large Research, Development and Innovations Infrastructures.

## APPENDIX A: SAMPLE AND RIXS MEASUREMENT

Single-domain single crystals of  $\text{Na}_2\text{IrO}_3$  are grown by the self-flux. Powders of  $\text{Na}_2\text{CO}_3$  are mixed with 10%–20% excess  $\text{IrO}_2$  and are calcined at 700 °C for 24 h. Single crystals are grown on top of a powder matrix in subsequent heating at 1050 °C. Platelike crystals with typical dimensions of 5 mm  $\times$  5 mm  $\times$  0.1 mm are physically extracted. The sample is mounted in a Displex closed-cycle cryostat. The RIXS measurements are performed using the RIXS spectrometer at the 27-ID beam line of the Advanced Photon Source where the sample, analyzer, and detector are positioned in the Rowland geometry. The diamond(111) high-heat-load monochromator reflects x rays from two in-line undulators into a high-resolution monochromator. The two-bounce monochromator of single monolithic Si(844) channel-cut crystal produces an energy bandpass of 14.8 meV. The four-bounce monochromator of two monolithic Si(844) channel-cut crystals results in an energy bandpass of 8.9 meV. The beam is then focused by a set of

Kirkpatrick-Baez mirrors, yielding a typical spot size of  $10 \times 40 \mu\text{m}^2$  FWHM ( $v \times h$ ) at the sample. A horizontal scattering geometry is used with the incident photon polarization in the scattering plane. Mapping of the full Brillouin zone is carried out within only a few degrees of  $90^\circ$  scattering geometry to minimize the contribution from the Thompson elastic scattering. For the 25 meV RIXS measurement, a Si(844) diced spherical analyzer with 1-in diameter and a position-sensitive silicon microstrip detector are used with the 14.8 meV incident bandpass. For the 12 meV RIXS measurement, a quartz(309) diced spherical analyzer with 1-in diameter is used with the 8.9 meV incident bandpass.

## APPENDIX B: EXACT DIAGONALIZATION ON FINITE CLUSTERS

The theoretical RIXS intensity is obtained by combining the components of the pseudospin susceptibility tensor calculated for zero temperature:

$$\chi_{\alpha\beta}(\mathbf{q}, \omega) = i \int_0^\infty \langle \text{GS} | [S_{\mathbf{q}}^\alpha(t), S_{-\mathbf{q}}^\beta(0)] | \text{GS} \rangle e^{i\omega t} dt, \quad (\text{B1})$$

where

$$S_{\mathbf{q}}^\alpha = \frac{1}{\sqrt{N_{\text{site}}}} \sum_{\mathbf{R}} S_{\mathbf{R}}^\alpha e^{-i\mathbf{q}\cdot\mathbf{R}}. \quad (\text{B2})$$

The ground state  $|\text{GS}\rangle$  and, subsequently, the dynamic response embodied in  $\chi_{\alpha\beta}(\mathbf{q}, \omega)$  are evaluated by the standard Lanczos exact diagonalization method [75] based on periodic tiling of the honeycomb lattice with small clusters. Since the intensity profiles contain broad features corresponding to continua of densely spaced levels, to achieve convergence, we use a large number of Lanczos steps in the calculation—500 to get the data in Fig. 4 and 1200 to get the fine-resolved data presented in Fig. 6. A combination of symmetric hexagonal clusters 24a and 32a and rectangular clusters 32b1–32b3 shown in Fig. 8 enable us to access a number of wave vectors along the  $\Gamma$ - $M$ - $\Gamma'$ - $X$ - $K$ - $\Gamma$ - $Y$ - $K'$ - $\Gamma'$  path used to plot the maps. The maps are constructed by nearest-point interpolation with an additional averaging if the given wave vector is compatible with several clusters.

To account for the simultaneous presence of the three zigzag patterns in the sample—one long-range and two short-range correlated [15]—the response for the three possibilities with different directions of zigzag chains needs to be averaged. This average is, in fact, automatically included in the exact diagonalization calculation, because the symmetry is not spontaneously broken and the cluster ground state is a superposition of the zigzag patterns (equal-weight superposition in the case of 24a and 32a and approximately equal-weight for 32b). The explicit

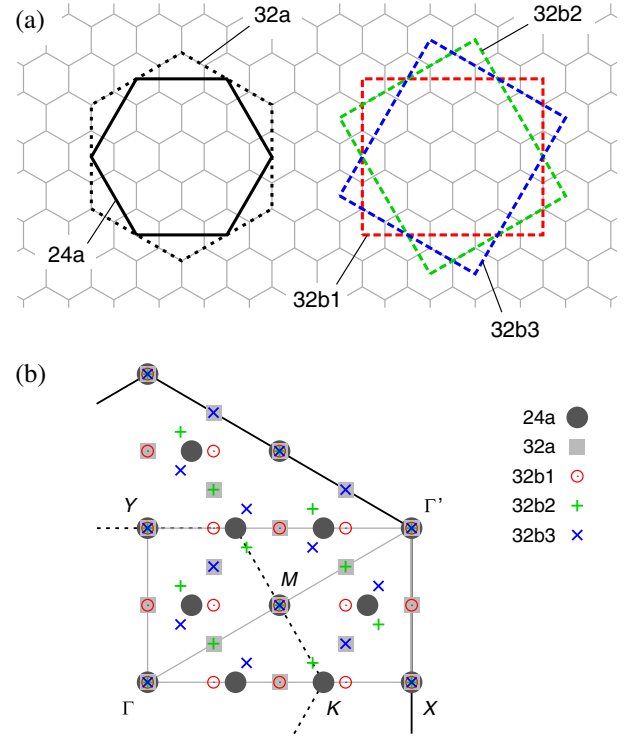


FIG. 8. (a) Clusters used in the exact diagonalization calculations: fully symmetric hexagonal 24- and 32-site clusters and a rectangular 32-site cluster in three possible orientations with respect to the honeycomb lattice. (b) Wave vectors compatible with periodic boundary conditions applied to the individual clusters. They are shown in one quadrant of the first Brillouin zone of the honeycomb lattice (dashed black line) and that of the completed triangular lattice (solid black line). High-symmetry points and the path along which the measured or simulated data are presented (gray line) are indicated [cf. Fig. 1(a)].

averaging is performed in the case of the linear spin-wave calculation only.

A side note on the selection of the clusters is in order: Even though there are other 24-site clusters (of elongated or asymmetric shape) that could bring better  $\mathbf{q}$  resolution, their dynamic response contains artifacts, e.g., due to the creation of very short zigzag chain loops of just a few bonds when periodic boundary conditions are applied. When compared to the dataset for 24a, 32a, and 32b, the corresponding intensity profiles clearly stand out and are thus not included as unreliable.

## APPENDIX C: HIDDEN HEISENBERG AND KITAEV POINTS

In this Appendix, we briefly elaborate on the points of hidden symmetry and the links between the excitation spectra of the extended Kitaev-Heisenberg model and the “hidden” models. The hidden-symmetry points are revealed by rotating spin axes, either globally or in a sublattice-dependent fashion, to convert the extended Kitaev-Heisenberg model

with a particular set of parameters to a simpler model [61]. This one-to-one correspondence enables us to transfer the known features such as the excitation spectra of the simpler model to the extended Kitaev-Heisenberg one.

We start with the hidden Kitaev point. To reveal its presence, one has to utilize the self-dual transformation [61] of the pseudospin Hamiltonian between the original axes  $xyz$  used in Eq. (1) and the new axes  $x'y'z'$  that are  $180^\circ$  rotated around the axis perpendicular to the honeycomb plane (see the insets in Fig. 9). The two reference frames for the spins are linked by the relation

$$\begin{pmatrix} S^{x'} \\ S^{y'} \\ S^{z'} \end{pmatrix} = \frac{1}{3} \begin{pmatrix} -1 & 2 & 2 \\ 2 & -1 & 2 \\ 2 & 2 & -1 \end{pmatrix} \begin{pmatrix} S^x \\ S^y \\ S^z \end{pmatrix}. \quad (\text{C1})$$

Applying the transformation to the case of Ising-type interaction in the new coordinate system  $x'y'z'$ , we find the correspondence

$$\begin{aligned} S_i^z S_j^z &= -\frac{1}{3} S_i^z S_j^z + \frac{4}{9} \mathbf{S}_i \cdot \mathbf{S}_j + \frac{4}{9} (S_i^x S_j^y + S_i^y S_j^x) \\ &\quad - \frac{2}{9} (S_i^x S_j^z + S_i^z S_j^x + S_i^y S_j^z + S_i^z S_j^y). \end{aligned} \quad (\text{C2})$$

The  $180^\circ$  rotation is compatible with the cyclic permutation among  $xyz$  and  $x'y'z'$  axes so that similar relations can be found for  $S_i^x S_j^y$  and  $S_i^y S_j^x$  interactions. Altogether, the Ising-type interaction distributed on  $x$ ,  $y$ , and  $z$  bonds constitutes the Kitaev model, while the right-hand side of the relation (C2) (and the two other ones) is just the extended Kitaev-Heisenberg model with a particular combination of parameters. Therefore, at the hidden Kitaev point given by the parameters  $J = \frac{4}{9} K_0$ ,  $K = -\frac{1}{3} K_0$ ,  $\Gamma = \frac{4}{9} K_0$ , and  $\Gamma' = -\frac{2}{9} K_0$ , the extended Kitaev-Heisenberg model exactly maps to a Kitaev model with the interaction constant  $K_0$ . Since the transformation is just a global rotation of the spin axes, all the features of the Kitaev model are exactly reproduced at the hidden Kitaev point. In particular, the excitation spectra are identical, and the spin susceptibility is obtained from that of the Kitaev model by a simple linear combination of the components.

The hidden Heisenberg point is given by the parameters  $J = -\frac{1}{9} J_0$ ,  $K = -\frac{2}{3} J_0$ ,  $\Gamma = \frac{8}{9} J_0$ , and  $\Gamma' = -\frac{4}{9} J_0$ , where  $J_0$  is the effective Heisenberg interaction constant. Here, the connection is less apparent, since, by applying the above global rotation (C1), we get to the Kitaev-Heisenberg model only. Its parameters read as  $K' = 2J_0$  and  $J' = -J_0$  ( $\Gamma$  and  $\Gamma'$  are zero). To establish the relation to the final Heisenberg model, we have to invoke the four-sublattice transformation connecting zigzag and Néel order [5,61,76]. It is depicted in Fig. 9(a) and consists of  $180^\circ$  rotations around one of the cubic axes or identity applied on the respective sublattices. This transformation preserves the

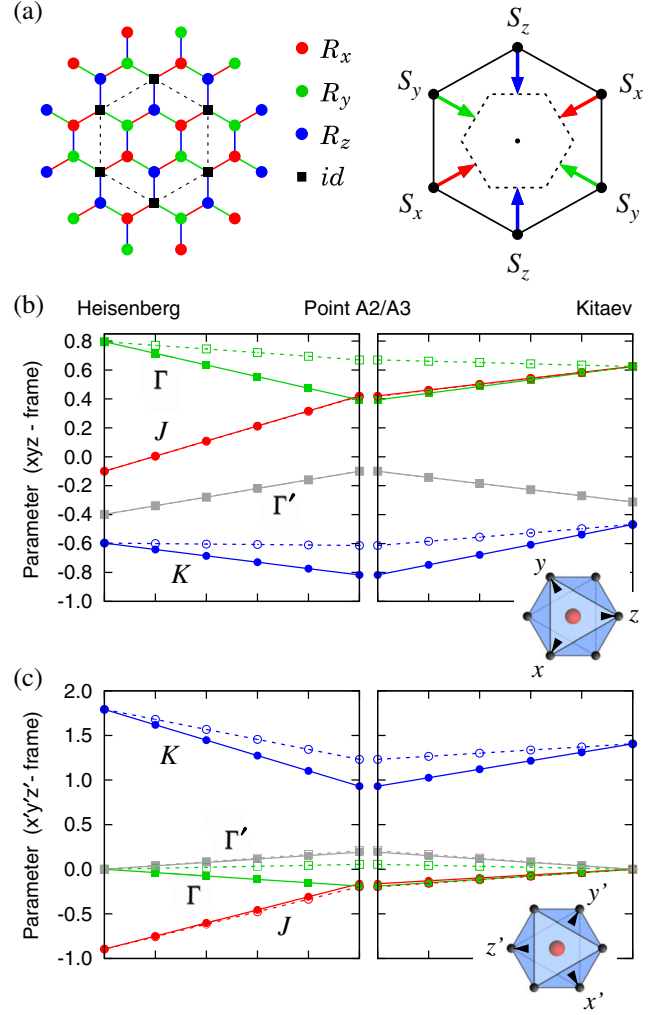


FIG. 9. (a) Four-sublattice transformation used in the text. At the individual sublattices, the spin axes are rotated by  $180^\circ$  around the cubic axes  $x$ ,  $y$ , and  $z$  or left intact. In the momentum space (right), the spin components are shifted by the zigzag ordering vectors. (b) Model parameter values along the lines used in Fig. 6. The values are expressed using the original  $xyz$ -coordinate system for the spins. The full lines and symbols correspond to Figs. 6(a) and 6(b), and dashed lines and open symbols to Figs. 6(c) and 6(d). The figure is organized like Fig. 6 with A2 or A3 parameters being in the middle and the evolution toward the hidden Heisenberg (Kitaev) point corresponding to the left (right) direction from the middle. Only nearest-neighbor interaction parameters  $JK\Gamma\Gamma'$  are presented;  $J_{2,3}$  linearly vanish when approaching the points of hidden symmetry. The marked parameter points correspond to the spectra shown in Fig. 6. (c) The same lines through the parameter space but expressed using the  $x'y'z'$ -coordinate system rotated by  $180^\circ$  around the axis perpendicular to the honeycomb plane. In both  $xyz$  and  $x'y'z'$  frames depicted by the insets, the axes point above the paper plane.

form of the Kitaev-Heisenberg model but changes the balance between the Kitaev and Heisenberg term and, for the above parameters  $K'$  and  $J'$ , leads to a pure Heisenberg model with the exchange parameter  $J_0$ . Again, all the

features of the Heisenberg model such as the magnon spectra can be transferred to the hidden Heisenberg point. However, due to the four-sublattice transformation, momentum shifts depicted in Fig. 9(a) are involved. The Fourier components of  $S^x$ ,  $S^y$ , and  $S^z$  are shifted by wave vectors with the directions identical to the corresponding bond directions of the honeycomb lattice [61]. The intense AFM Heisenberg magnons residing at the  $\Gamma'$  points in the corners of the extended Brillouin zone are then translated to the zigzag  $M$  points.

In the main text, we study the parameter evolution of the  $\mathbf{q} = 0$  spectra when going toward the hidden Heisenberg and Kitaev points. The corresponding parameter values are shown in Fig. 9(b) in the  $xyz$  reference frame and in Fig. 9(c) also rotated via Eq. (C1) to the  $x'y'z'$  reference frame. Note that, in the  $x'y'z'$  frame, the dominant interaction at our points  $A2$  and  $A3$  is  $K > 0$ , accompanied by small  $J < 0$  and  $\Gamma$  and  $\Gamma'$  interactions. The calculated response is thus similar to the one obtained for the upper zigzag phase in Fig. 3 that is stabilized in the Kitaev-Heisenberg model itself.

- 
- [1] A. Kitaev, *Anyons in an Exactly Solved Model and Beyond*, *Ann. Phys. (Amsterdam)* **321**, 2 (2006).
- [2] S. R. Elliott and M. Franz, *Colloquium: Majorana Fermions in Nuclear, Particle, and Solid-State Physics*, *Rev. Mod. Phys.* **87**, 137 (2015).
- [3] A. Yu. Kitaev, *Fault-Tolerant Quantum Computation by Anyons*, *Ann. Phys. (Amsterdam)* **303**, 2 (2003).
- [4] G. Jackeli and G. Khaliullin, *Mott Insulators in the Strong Spin-Orbit Coupling Limit: From Heisenberg to a Quantum Compass and Kitaev Models*, *Phys. Rev. Lett.* **102**, 017205 (2009).
- [5] J. Chaloupka, G. Jackeli, and G. Khaliullin, *Kitaev-Heisenberg Model on a Honeycomb Lattice: Possible Exotic Phases in Iridium Oxides  $A_2\text{IrO}_3$* , *Phys. Rev. Lett.* **105**, 027204 (2010).
- [6] I. Kimchi and Y.-Z. You, *Kitaev-Heisenberg- $J_2$ - $J_3$  Model for the Iridates  $A_2\text{IrO}_3$* , *Phys. Rev. B* **84**, 180407(R) (2011).
- [7] J. G. Rau, E. K.-H. Lee, and H.-Y. Kee, *Generic Spin Model for the Honeycomb Iridates beyond the Kitaev Limit*, *Phys. Rev. Lett.* **112**, 077204 (2014).
- [8] Y. Yamaji, Y. Nomura, M. Kurita, R. Arita, and M. Imada, *First-Principles Study of the Honeycomb-Lattice Iridates  $\text{Na}_2\text{IrO}_3$  in the Presence of Strong Spin-Orbit Interaction and Electron Correlations*, *Phys. Rev. Lett.* **113**, 107201 (2014).
- [9] K. Shinjo, S. Sota, and T. Tohyama, *Density-Matrix Renormalization Group Study of the Extended Kitaev-Heisenberg Model*, *Phys. Rev. B* **91**, 054401 (2015).
- [10] E. Sela, H.-C. Jiang, M. H. Gerlach, and S. Trebst, *Order-by-Disorder and Spin-Orbital Liquids in a Distorted Heisenberg-Kitaev Model*, *Phys. Rev. B* **90**, 035113 (2014).
- [11] Y. Singh and P. Gegenwart, *Antiferromagnetic Mott Insulating State in Single Crystals of the Honeycomb Lattice Material  $\text{Na}_2\text{IrO}_3$* , *Phys. Rev. B* **82**, 064412 (2010).
- [12] X. Liu, T. Berlijn, W.-G. Yin, W. Ku, A. Tsvelik, Y.-J. Kim, H. Gretarsson, Y. Singh, P. Gegenwart, and J. P. Hill, *Long-Range Magnetic Ordering in  $\text{Na}_2\text{IrO}_3$* , *Phys. Rev. B* **83**, 220403(R) (2011).
- [13] F. Ye, S. Chi, H. Cao, B. C. Chakoumakos, J. A. Fernandez-Baca, R. Custelcean, T. F. Qi, O. B. Korneta, and G. Cao, *Direct Evidence of a Zigzag Spin-Chain Structure in the Honeycomb Lattice: A Neutron and x-ray Diffraction Investigation of Single-Crystal  $\text{Na}_2\text{IrO}_3$* , *Phys. Rev. B* **85**, 180403(R) (2012).
- [14] S. K. Choi, R. Coldea, A. N. Kolmogorov, T. Lancaster, I. I. Mazin, S. J. Blundell, P. G. Radaelli, Y. Singh, P. Gegenwart, K. R. Choi, S.-W. Cheong, P. J. Baker, C. Stock, and J. Taylor, *Spin Waves and Revised Crystal Structure of Honeycomb Iridate  $\text{Na}_2\text{IrO}_3$* , *Phys. Rev. Lett.* **108**, 127204 (2012).
- [15] S. H. Chun, J.-W. Kim, J. Kim, H. Zheng, C. Stoumpos, C. Malliakas, J. F. Mitchell, K. Mehlawat, Y. Singh, Y. Choi, T. Gog, A. Al-Zein, M. M. Sala, M. Krisch, J. Chaloupka, G. Jackeli, G. Khaliullin, and B. J. Kim, *Direct Evidence for Dominant Bond-Directional Interactions in a Honeycomb Lattice Iridate  $\text{Na}_2\text{IrO}_3$* , *Nat. Phys.* **11**, 462 (2015).
- [16] V. M. Katukuri, S. Nishimoto, V. Yushankhai, A. Stoyanova, H. Kandpal, S. Choi, R. Coldea, I. Rousochatzakis, L. Hozoi, and J. van den Brink, *Kitaev Interactions between  $J = 1/2$  Moments in Honeycomb  $\text{Na}_2\text{IrO}_3$  are Large and Ferromagnetic: Insights from ab initio Quantum Chemistry Calculations*, *New J. Phys.* **16**, 013056 (2014).
- [17] S. M. Winter, Y. Li, H. O. Jeschke, and R. Valentí, *Challenges in Design of Kitaev Materials: Magnetic Interactions from Competing Energy Scales*, *Phys. Rev. B* **93**, 214431 (2016).
- [18] S. M. Winter, A. A. Tsirlin, M. Daghofer, J. van den Brink, Y. Singh, P. Gegenwart, and R. Valentí, *Models and Materials for Generalized Kitaev Magnetism*, *J. Phys. Condens. Matter* **29**, 493002 (2017).
- [19] I. Rousochatzakis and N. B. Perkins, *Classical Spin Liquid Instability Driven by Off-Diagonal Exchange in Strong Spin-Orbit Magnets*, *Phys. Rev. Lett.* **118**, 147204 (2017).
- [20] M. Gohlke, G. Wachtel, Y. Yamaji, F. Pollmann, and Y. B. Kim, *Quantum Spin Liquid Signatures in Kitaev-Like Frustrated Magnets*, *Phys. Rev. B* **97**, 075126 (2018).
- [21] Y. Singh, S. Manni, J. Reuther, T. Berlijn, R. Thomale, W. Ku, S. Trebst, and P. Gegenwart, *Relevance of the Heisenberg-Kitaev Model for the Honeycomb Lattice Iridates  $A_2\text{IrO}_3$* , *Phys. Rev. Lett.* **108**, 127203 (2012).
- [22] T. Takayama, A. Kato, R. Dinnebier, J. Nuss, H. Kono, L. S. I. Veiga, G. Fabbri, D. Haskel, and H. Takagi, *Hyperhoneycomb Iridate  $\beta\text{-Li}_2\text{IrO}_3$  as a Platform for Kitaev Magnetism*, *Phys. Rev. Lett.* **114**, 077202 (2015).
- [23] K. A. Modic, T. E. Smidt, I. Kimchi, N. P. Breznay, A. Biffin, S. Choi, R. D. Johnson, R. Coldea, P. Watkins-Curry, G. T. McCandless, J. Y. Chan, F. Gandara, Z. Islam, A. Vishwanath, A. Shekhter, R. D. McDonald, and J. G. Analytis, *Realization of a Three-Dimensional Spin-Anisotropic Harmonic Honeycomb Iridate*, *Nat. Commun.* **5**, 4203 (2014).
- [24] M. Abramchuk, C. Ozsoy-Keskinbora, J. W. Krizan, K. R. Metz, D. C. Bell, and F. Tafti,  *$\text{Cu}_2\text{IrO}_3$ : A New Magnetically*

- Frustrated Honeycomb Iridate*, *J. Am. Chem. Soc.* **139**, 15371 (2017).
- [25] K. Kitagawa, T. Takayama, Y. Matsumoto, A. Kato, R. Takano, Y. Kishimoto, S. Bette, R. Dinnebier, G. Jackeli, and H. Takagi, *A Spin–Orbital-Entangled Quantum Liquid on a Honeycomb Lattice*, *Nature (London)* **554**, 341 (2018).
- [26] K. W. Plumb, J. P. Clancy, L. J. Sandilands, V. V. Shankar, Y. F. Hu, K. S. Burch, H.-Y. Kee, and Y.-J. Kim,  *$\alpha$ -RuCl<sub>3</sub>: A Spin-Orbit Assisted Mott Insulator on a Honeycomb*, *Phys. Rev. B* **90**, 041112(R) (2014).
- [27] A. Banerjee, C. A. Bridges, J.-Q. Yan, A. A. Aczel, L. Li, M. B. Stone, G. E. Granroth, M. D. Lumsden, Y. Yiu, J. Knolle, S. Bhattacharjee, D. L. Kovrizhin, R. Moessner, D. A. Tennant, D. G. Mandrus, and S. E. Nagler, *Proximate Kitaev Quantum Spin Liquid Behaviour in a Honeycomb Magnet*, *Nat. Mater.* **15**, 733 (2016).
- [28] K. Ran, J. Wang, W. Wang, Z.-Y. Dong, X. Ren, S. Bao, S. Li, Z. Ma, Y. Gan, Y. Zhang, J. T. Park, G. Deng, S. Danilkin, S.-L. Yu, J.-X. Li, and J. Wen, *Spin-Wave Excitations Evidencing the Kitaev Interaction in Single Crystalline  $\alpha$ -RuCl<sub>3</sub>*, *Phys. Rev. Lett.* **118**, 107203 (2017).
- [29] A. Banerjee, J. Yan, J. Knolle, C. A. Bridges, M. B. Stone, M. D. Lumsden, D. G. Mandrus, D. A. Tennant, R. Moessner, and S. E. Nagler, *Neutron Scattering in the Proximate Quantum Spin Liquid  $\alpha$ -RuCl<sub>3</sub>*, *Science* **356**, 1055 (2017).
- [30] S.-H. Do, S.-Y. Park, J. Yoshitake, J. Nasu, Y. Motome, Y. S. Kwon, D. T. Adroja, D. J. Voneshen, K. Kim, T.-H. Jang, J.-H. Park, K.-Y. Choi, and S. Ji, *Majorana Fermions in the Kitaev Quantum Spin System  $\alpha$ -RuCl<sub>3</sub>*, *Nat. Phys.* **13**, 1079 (2017).
- [31] M. E. Zhitomirsky and A. L. Chernyshev, *Colloquium: Spontaneous Magnon Decays*, *Rev. Mod. Phys.* **85**, 219 (2013).
- [32] S. M. Winter, K. Riedl, P. A. Maksimov, A. L. Chernyshev, A. Honecker, and R. Valentí, *Breakdown of Magnons in a Strongly Spin-Orbital Coupled Magnet*, *Nat. Commun.* **8**, 1152 (2017).
- [33] L. J. Sandilands, Y. Tian, K. W. Plumb, Y.-J. Kim, and K. S. Burch, *Scattering Continuum and Possible Fractionalized Excitations in  $\alpha$ -RuCl<sub>3</sub>*, *Phys. Rev. Lett.* **114**, 147201 (2015).
- [34] J. Nasu, J. Knolle, D. L. Kovrizhin, Y. Motome, and R. Moessner, *Fermionic Response from Fractionalization in an Insulating Two-Dimensional Magnet*, *Nat. Phys.* **12**, 912 (2016).
- [35] J. Yoshitake, J. Nasu, and Y. Motome, *Fractional Spin Fluctuations as a Precursor of Quantum Spin Liquids: Majorana Dynamical Mean-Field Study for the Kitaev Model*, *Phys. Rev. Lett.* **117**, 157203 (2016).
- [36] I. A. Leahy, C. A. Pocs, P. E. Siegfried, D. Graf, S.-H. Do, K.-Y. Choi, B. Normand, and M. Lee, *Anomalous Thermal Conductivity and Magnetic Torque Response in the Honeycomb Magnet  $\alpha$ -RuCl<sub>3</sub>*, *Phys. Rev. Lett.* **118**, 187203 (2017).
- [37] M. Gohlke, R. Verresen, R. Moessner, and F. Pollmann, *Dynamics of the Kitaev-Heisenberg Model*, *Phys. Rev. Lett.* **119**, 157203 (2017).
- [38] S. N. Gupta, P. V. Sriluckshmy, K. Mehlawat, A. Balodhi, D. K. Mishra, S. R. Hassan, T. V. Ramakrishnan, D. V. S. Muthu, Y. Singh, and A. K. Sood, *Raman signatures of strong Kitaev exchange correlations in (Na<sub>1-x</sub>Li<sub>x</sub>)<sub>2</sub>IrO<sub>3</sub>: Experiments and theory*, *Europhys. Lett.* **114**, 47004 (2016).
- [39] J. Knolle, G.-W. Chern, D. L. Kovrizhin, R. Moessner, and N. B. Perkins, *Raman Scattering Signatures of Kitaev Spin Liquids in A<sub>2</sub>IrO<sub>3</sub> Iridates with A = Na or Li*, *Phys. Rev. Lett.* **113**, 187201 (2014).
- [40] K. Mehlawat, A. Thamizhavel, and Y. Singh, *Heat Capacity Evidence for Proximity to the Kitaev Quantum Spin Liquid in A<sub>2</sub>IrO<sub>3</sub> (A = Na, Li)*, *Phys. Rev. B* **95**, 144406 (2017).
- [41] I. A. Leahy, C. A. Pocs, P. E. Siegfried, D. Graf, S.-H. Do, K.-Y. Choi, B. Normand, and M. Lee, *Anomalous Thermal Conductivity and Magnetic Torque Response in the Honeycomb Magnet  $\alpha$ -RuCl<sub>3</sub>*, *Phys. Rev. Lett.* **118**, 187203 (2017).
- [42] S. D. Das, S. Kundu, Z. Zhu, E. Mun, R. D. McDonald, G. Li, L. Balicas, A. McCollam, G. Cao, J. G. Rau, H.-Y. Kee, V. Tripathi, and S. E. Sebastian, *Magnetic Anisotropy of the Alkali Iridate Na<sub>2</sub>IrO<sub>3</sub> at High Magnetic Fields: Evidence for Strong Ferromagnetic Kitaev Correlations*, *Phys. Rev. B* **99**, 081101(R) (2019).
- [43] H. Gretarsson, J. P. Clancy, Y. Singh, P. Gegenwart, J. P. Hill, J. Kim, M. H. Upton, A. H. Said, D. Casa, T. Gog, and Y.-J. Kim, *Magnetic Excitation Spectrum of Na<sub>2</sub>IrO<sub>3</sub> Probed with Resonant Inelastic x-ray Scattering*, *Phys. Rev. B* **87**, 220407(R) (2013).
- [44] A. Revelli, M. M. Sala, G. Monaco, C. Hickey, P. Becker, F. Freund, A. Jesche, P. Gegenwart, T. Eschmann, F. L. Buessen, S. Trebst, P. H. M. van Loosdrecht, J. van den Brink, and M. Gruninger, *Fingerprints of Kitaev Physics in the Magnetic Excitations of Honeycomb Iridates* arXiv:1905.13590.
- [45] A. H. Said, T. Gog, M. Wiczorek, X. Huang, D. Casa, E. Kasman, R. Divan, and J. H. Kim, *High-Energy-Resolution Diced Spherical Quartz Analyzers for Resonant Inelastic X-ray Scattering*, *J. Synchrotron Radiat.* **25**, 373 (2018).
- [46] J. Kim, D. Casa, A. Said, R. Krakora, B. J. Kim, E. Kasman, X. Huang, and T. Gog, *Quartz-Based Flat-Crystal Resonant Inelastic x-ray Scattering Spectrometer with sub-10 meV Energy Resolution*, *Sci. Rep.* **8**, 1958 (2018).
- [47] T. Gog, D. M. Casa, A. H. Said, M. H. Upton, J. Kim, I. Kuzmenko, X. Huang, and R. Khachatryan, *Spherical Analyzers and Monochromators for Resonant Inelastic Hard X-ray Scattering: A Compilation of Crystals and Reflections*, *J. Synchrotron Radiat.* **20**, 74 (2013).
- [48] Yu. V. Shvyd'ko, J. P. Hill, C. A. Burns, D. S. Coburn, B. Brajuskovic, D. Casa, K. Goetze, T. Gog, R. Khachatryan, J.-H. Kim, C. N. Koditwakku, M. Ramanathan, T. Roberts, A. Said, H. Sinn, D. Shu, S. Stoupin, M. Upton, M. Wiczorek, and H. Yavas, *Merix—Next Generation Medium Energy Resolution Inelastic X-Ray Scattering Instrument at the APS*, *J. Electron Spectrosc. Relat. Phenom.* **188**, 140 (2013).
- [49] R. Comin, G. Levy, B. Ludbrook, Z.-H. Zhu, C. N. Veenstra, J. A. Rosen, Y. Singh, P. Gegenwart, D. Stricker, J. N. Hancock, D. van der Marel, I. S. Elfimov, and A. Damascelli, *Na<sub>2</sub>IrO<sub>3</sub> as a Novel Relativistic Mott Insulator with a 340-meV Gap*, *Phys. Rev. Lett.* **109**, 266406 (2012).
- [50] J. G. Rau and H.-Y. Kee, *Trigonal Distortion in the Honeycomb Iridates: Proximity of Zigzag And Spiral Phases in Na<sub>2</sub>IrO<sub>3</sub>*, arXiv:1408.4811.

- [51] J. Chaloupka and G. Khaliullin, *Magnetic Anisotropy in the Kitaev Model Systems  $\text{Na}_2\text{IrO}_3$  and  $\text{RuCl}_3$* , *Phys. Rev. B* **94**, 064435 (2016).
- [52] B. J. Kim and G. Khaliullin, *Resonant Inelastic x-ray Scattering Operators for  $t_{2g}$  Orbital Systems*, *Phys. Rev. B* **96**, 085108 (2017).
- [53] H. Gretarsson, J. P. Clancy, X. Liu, J. P. Hill, E. Bozin, Y. Singh, S. Manni, P. Gegenwart, J. Kim, A. H. Said, D. Casa, T. Gog, M. H. Upton, H.-S. Kim, J. Yu, V. M. Katukuri, L. Hozoi, J. van den Brink, and Y.-J. Kim, *Crystal-Field Splitting and Correlation Effect on the Electronic Structure of  $\text{A}_2\text{IrO}_3$* , *Phys. Rev. Lett.* **110**, 076402 (2013).
- [54] J. Rusnačko, D. Gotfryd, and J. Chaloupka, *Structural and Magnetic Studies of  $\text{Sr}_2\text{IrO}_4$* , *Phys. Rev. B* **99**, 064425 (2019).
- [55] H. Gretarsson, N. H. Sung, M. Höppner, B. J. Kim, B. Keimer, and M. Le Tacon, *Two-Magnon Raman Scattering and Pseudospin-Lattice Interactions in  $\text{Sr}_2\text{IrO}_4$  and  $\text{Sr}_3\text{Ir}_2\text{O}_7$* , *Phys. Rev. Lett.* **116**, 136401 (2016).
- [56] H. Gretarsson, J. Saucedo, N. H. Sung, M. Höppner, M. Minola, B. J. Kim, B. Keimer, and M. Le Tacon, *Raman Scattering Study of Vibrational and Magnetic Excitations in  $\text{Sr}_{2-x}\text{La}_x\text{IrO}_4$* , *Phys. Rev. B* **96**, 115138 (2017).
- [57] L. Braicovich, M. Rossi, R. Fumagalli, Y. Peng, Y. Wang, R. Arpaia, D. Betto, G. M. D. Luca, D. D. Castro, K. Kummer, M. M. Sala, M. Pagetti, G. Balestrino, N. B. Brookes, M. Salluzzo, S. Johnston, J. van den Brink, and G. Ghiringhelli, *Determining the Electron-Phonon Coupling in Superconducting Cuprates by Resonant Inelastic X-ray Scattering: Methods and Results on  $\text{Nd}_{1+x}\text{Ba}_{2-x}\text{Cu}_3\text{O}_{7-\delta}$*  arXiv: 1906.01270.
- [58] M. O. Krause and J. H. Oliver, *Natural Widths of Atomic K and L Levels, K $\alpha$  X-ray Lines and Several KLL Auger Lines*, *J. Phys. Chem. Ref. Data* **8**, 329 (1979).
- [59] V. Hermann, J. Ebad-Allah, F. Freund, I. M. Pietsch, A. Jesche, A. A. Tsirlin, J. Deisenhofer, M. Hanfland, P. Gegenwart, and C. A. Kuntscher, *High-Pressure versus Isoelectronic Doping Effect on the Honeycomb Iridate  $\text{Na}_2\text{IrO}_3$* , *Phys. Rev. B* **96**, 195137 (2017).
- [60] J. G. Vale, C. D. Dashwood, E. Paris, L. S. I. Veiga, M. Garcia-Fernandez, A. Nag, A. Walters, K. J. Zhou, I. M. Pietsch, A. Jesche, P. Gegenwart, R. Coldea, T. Schmitt, and D. F. McMorrow, *High-Resolution Resonant Inelastic x-ray Scattering study of the Electron-Phonon Coupling in Honeycomb  $\alpha\text{-Li}_2\text{IrO}_3$* , *Phys. Rev. B* **100**, 224303 (2019).
- [61] J. Chaloupka and G. Khaliullin, *Hidden Symmetries of the Extended Kitaev-Heisenberg Model: Implications for the Honeycomb-Lattice Iridates  $\text{A}_2\text{IrO}_3$* , *Phys. Rev. B* **92**, 024413 (2015).
- [62] J. Chaloupka, G. Jackeli, and G. Khaliullin, *Zigzag Magnetic Order in the Iridium Oxide  $\text{Na}_2\text{IrO}_3$* , *Phys. Rev. Lett.* **110**, 097204 (2013).
- [63] J. Knolle, D. L. Kovrizhin, J. T. Chalker, and R. Moessner, *Dynamics of Fractionalization in Quantum Spin Liquids*, *Phys. Rev. B* **92**, 115127 (2015).
- [64] D. Gotfryd, J. Rusnačko, K. Wohlfeld, G. Jackeli, J. Chaloupka, and A. M. Oleš, *Phase Diagram and Spin Correlations of the Kitaev-Heisenberg Model: Importance of Quantum Effects*, *Phys. Rev. B* **95**, 024426 (2017).
- [65] J. Knolle, D. L. Kovrizhin, J. T. Chalker, and R. Moessner, *Dynamics of a Two-Dimensional Quantum Spin Liquid: Signatures of Emergent Majorana Fermions and Fluxes*, *Phys. Rev. Lett.* **112**, 207203 (2014).
- [66] J. Knolle, S. Bhattacharjee, and R. Moessner, *Dynamics of a Quantum Spin Liquid Beyond Integrability: The Kitaev-Heisenberg- $\Gamma$  Model in an Augmented Parton Mean-Field Theory*, *Phys. Rev. B* **97**, 134432 (2018).
- [67] J. Wang, B. Normand, and Z.-X. Liu, *One Proximate Kitaev Spin Liquid in the K-J- $\Gamma$  Model on the Honeycomb Lattice*, *Phys. Rev. Lett.* **123**, 197201 (2019).
- [68] J. Nasu, M. Udagawa, and Y. Motome, *Thermal Fractionalization Of Quantum Spins in a Kitaev Model: Temperature-Linear Specific Heat and Coherent Transport of Majorana Fermions*, *Phys. Rev. B* **92**, 115122 (2015).
- [69] A. Catuneanu, Y. Yamaji, G. Wachtel, Y. B. Kim, and H.-Y. Kee, *Path to Stable Quantum Spin Liquids in Spin-Orbit Coupled Correlated Materials*, *npj Quantum Mater.* **3**, 23 (2018).
- [70] J. Yoshitake, J. Nasu, Y. Kato, and Y. Motome, *Majorana Dynamical Mean-Field Study of Spin Dynamics at Finite Temperatures in the Honeycomb Kitaev Model*, *Phys. Rev. B* **96**, 024438 (2017).
- [71] Y. Yamaji, T. Suzuki, T. Yamada, S.-I. Suga, N. Kawashima, and M. Imada, *Clues and Criteria for Designing a Kitaev Spin Liquid Revealed by Thermal and Spin Excitations of the Honeycomb Iridate  $\text{Na}_2\text{IrO}_3$* , *Phys. Rev. B* **93**, 174425 (2016).
- [72] G. B. Halász, N. B. Perkins, and J. van den Brink, *Resonant Inelastic X-Ray Scattering Response of the Kitaev Honeycomb Model*, *Phys. Rev. Lett.* **117**, 127203 (2016).
- [73] K. Ishii, S. Ishihara, Y. Murakami, K. Ikeuchi, K. Kuzushita, T. Inami, K. Ohwada, M. Yoshida, I. Jarrige, N. Tatami, S. Niioka, D. Bizen, Y. Ando, J. Mizuki, S. Maekawa, and Y. Endoh, *Polarization-Analyzed Resonant Inelastic x-ray Scattering of the Orbital Excitations in  $\text{KCuF}_3$* , *Phys. Rev. B* **83**, 241101(R) (2011).
- [74] X. Gao, D. Casa, J. Kim, T. Gog, C. Li, and C. Burns, *Toroidal Silicon Polarization Analyzer for Resonant Inelastic x-ray Scattering*, *Rev. Sci. Instrum.* **87**, 083107 (2016).
- [75] A. Avella and F. Mancini, *Strongly Correlated Systems: Numerical Methods* (Springer, Berlin, 2013).
- [76] G. Khaliullin, *Orbital Order and Fluctuations in Mott Insulators*, *Prog. Theor. Phys. Suppl.* **160**, 155 (2005).